CHALMERS
UNIVERSITY OF TECHNOLOGY

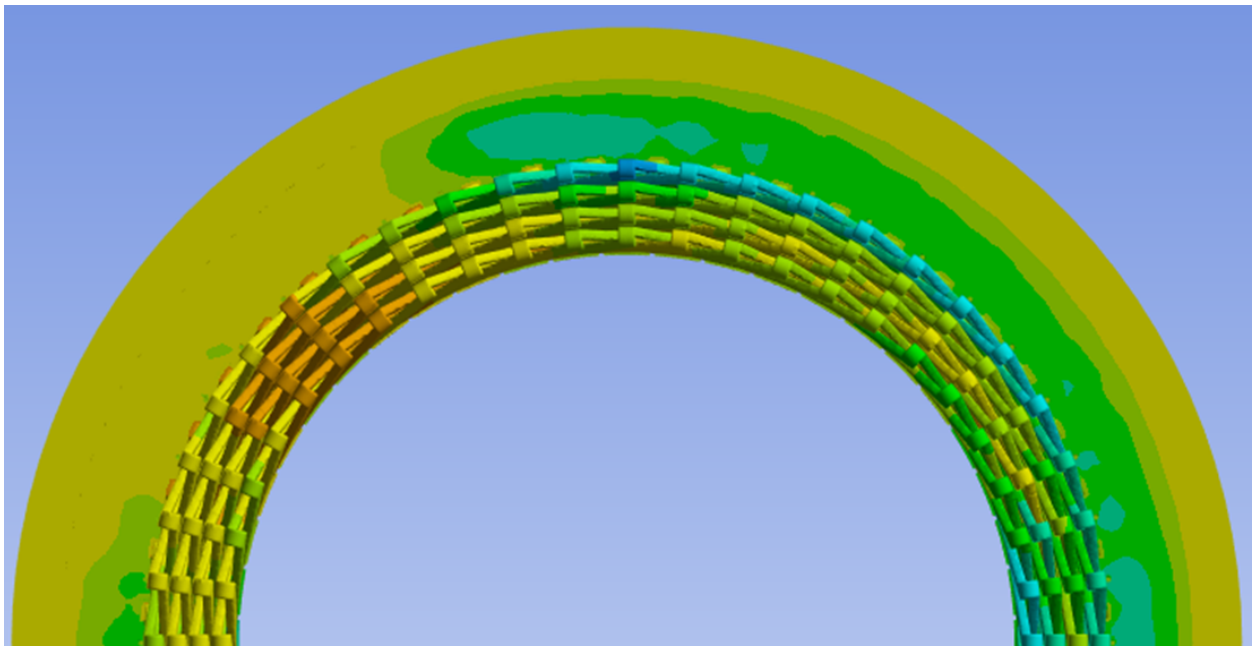

Thermal and Mechanical Design and Manufacturing of Electrically Excited Synchronous Machine for High-Speed applications

Master's thesis in Electrical Engineering

TANMAY MOTHARKAR

DEPARTMENT OF ELECTRICAL ENGINEERING

CHALMERS UNIVERSITY OF TECHNOLOGY
Gothenburg, Sweden 2024
www.chalmers.se

Master's thesis 2024

Thermal and Mechanical Design and Manufacturing of Electrically Excited Synchronous Machine for High-Speed applications

TANMAY MOTHARKAR

CHALMERS
UNIVERSITY OF TECHNOLOGY

Department of Electrical Engineering
Division of Electric Power Engineering
Chalmers University of Technology
Gothenburg, Sweden 2024

Thermal and Mechanical Design and Manufacturing of Electrically Excited Synchronous Machine for High-Speed applications
TANMAY MOTHARKAR

Supervisor: Luca Boscaglia, Department of Electrical Engineering
Examiner: Yujing Liu, Department of Electrical Engineering

Master's Thesis 2024
Department of Electrical Engineering
Division of Electric Power Engineering

Chalmers University of Technology
SE-412 96 Gothenburg
Telephone +46 31 772 1000

Cover: Thermal and Mechanical Design and Manufacturing of Electrically Excited Synchronous Machine for High-Speed applications.

Gothenburg, Sweden 2024

Thermal and Mechanical Design and Manufacturing of Electrically Excited Synchronous Machine for High-Speed applications
TANMAY MOTHARKAR
Department of Electrical Engineering
Chalmers University of Technology

Abstract

This thesis delves into the operational dynamics of Electrically Excited Synchronous Machines (EESMs), which are increasingly favored in high-speed applications due to their controllable rotor flux characteristics. However, high-speed operation introduces significant challenges, including the cooling of the rotor and end windings, as well as ensuring the mechanical integrity of joints under substantial centrifugal forces. This study aims to thoroughly investigate various losses inherent in EESMs, namely copper losses, iron losses, and mechanical losses, alongside the design and optimization of a cooling circuit specifically for the end winding. A comprehensive analysis employing Computational Fluid Dynamics (CFD) simulations was undertaken to evaluate different duct designs for cooling efficiency. These simulations varied flow rates to determine the most effective duct design based on key parameters such as outlet velocity, flow rate, and the pressure head required for coolant pumping. Among the designs evaluated, an elliptical-shaped duct emerged as the most efficient, offering optimal cooling by balancing the flow rate and minimizing resistance, thereby enhancing the overall performance and reliability of EESMs in high-speed applications. This research not only contributes to the advancement of EESM technology but also provides a framework for future exploration in the optimization of cooling systems within high-speed electric machinery.

Keywords: Electrically Excited Synchronous Machine(EESM), high-speed operation copper losses, iron losses, mechanical losses, cooling circuit.

Acknowledgements

I extend my heartfelt gratitude to my supervisor, Luca Boscaglia, for his invaluable assistance with CFD simulations and advice that significantly enhanced the professionalism of my work. Additionally, I am deeply thankful to my examiner, Prof. Yujing Liu, for his prompt approvals and diligent assessment of my master's thesis timeline, facilitating a smooth and efficient progression of my research. I would also like to acknowledge the collaboration with Polestar on this thesis, expressing my sincere appreciation to the employees at Polestar who provided insightful advice during our meetings. I am also grateful to the Department of Electrical Engineering, especially the Division of Electric Power Engineering, as well as the Department of Mechanics and Maritime Sciences, for the valuable learning opportunities they have offered. Their contributions have been instrumental in shaping the direction and success of my work.

Tanmay Motharkar, Gothenburg, September 2024

List of Acronyms

Below is the list of acronyms that have been used throughout this thesis :

EESM	Electrically Excited Synchronous Machine
CFD	Computational Fluid Dynamics
PMSM	Permanent Magnet Synchronous Machin
NdFeB	Neodymium-Iron-Boron
SIMPLE	Semi-Implicit Method for Pressure Linked Equations
NDE	Non-Driver-End
DE	Driver-End
FEA	Finite Element Analysis
CAD	Computer-Aided Design
TDH	Total Dynamic Head
HTC	Heat Transfer Coefficient
MPS	Moving Particle Simulation
OP	Operating Point
CAD	Computer Aided Design
SOC	State of Charge
OCV	Open Circuit Voltage
WLTC	Worldwide Harmonized Light Vehicles Test Cycle
GR	Gear Ratio

Nomenclature

Below is the list of abbreviations that have been used throughout this thesis :

Abbreviations

Q_{lm}	Flow Rate
Q_{ms}	amount of fluid flowing
V_t	Total Volume
N_s	Number of Slots in the Machine
S_y	Height of the Stator Cooling Slot
v_y	Initial Velocity of the Fluid in Y Direction
t	Time
v_x	Initial Velocity of the Fluid in Y Direction
S_x	Coolant Stream Distance in X Direction
H_p	Pressure Head
H_f	Friction Head
H_d	Discharge Head
P	Pressure
g	Acceleration due to Gravity
L	length of the pipe
D	Diameter of pipe at outlet
v	Velocity at outlet
g	Acceleration due to gravity
ρ	Density of coolant
f	Friction factor
k	Fitting factor for bends
z_2	Height of the outlet
z_1	Height of the inlet

w_{mc}	Width of Main Channel
t_h	Thickness of Housing
h_{mc}	Height of Main Channel
h_{2c}	Height of Type 2 Channel
h_c	Height of Type 1 Channel
L_1	Lamination length for Type 1 Channel
L_2	Lamination length for Type 2 Channel
L_3	Lamination length for Type 3 Channel
h	Heat Transfer Coefficient(HTC)
R	Resistance of the Material
A	Surface Area in Contact
h_t	Final HTC of the Coolant and Insulation
h_{oil}	HTC for oil
t_{ins}	Thickness of the Enamel Layer
R_{sl}	Thermal Resistance of the Slot Liner
L_{sl}	Thickness of the Slot Liner
K_{sl}	Thermal Conductivity of the Slot Liner
A_{sl}	Surface Area of the Slot Liner
C_{sl}	Thermal Conductivity of the Slot Liner
C_{sl}	Thermal Conductivity of the Slot Liner
F_t	Force by Pure Acceleration
m	Mass of Vehicle
a	Vehicle Acceleration
F_d	Aerodynamic Drag Force
C_d	Drag Coefficient
ρ_a	Air Density
A_r	Reference Area
u	Velocity of the Vehicle
F_g	Gradient Force on Vehicle
θ	Road Inclination
F_f	Frictional Force on Vehicle
F_n	Normal Force
μ	Coefficient of Friction
F_{netl}	Net Force on Vehicle

F_w	Force at Wheel
T_{wheel}	Torque at Wheel
r_{wheel}	Radius of Wheel
v_{wheel}	Velocity of Wheel
w_{wheel}	Angular Velocity of Wheel
a_{wheel}	Acceleration of Wheel
α	Angular Acceleration of Wheel
GR	Gear Ratio
N_{motor}	Rotational Speed of Motor
N_{wheel}	Rotational Speed of Wheel
T_{motor}	Torque of Motor
w_{motor}	Angular Velocity of Motor
$I_{battery}$	Battery Current
$P_{(battery}$	Battery Power
$V_{(battery}$	Battery Voltage
$V_{(terminal}$	Battery Terminal Voltage
$V_{(oc}$	Open Circuit Voltage
$R_{(int}$	Battery Internal Resistance
$I_{(cell}$	Cell Current
$N_{(parallel}$	Number of Cells in Parallel
$Q_{(used}$	Total Charge
τ	Time
$Q_{(remaining}$	Charge Remaining
$Q_{(initial}$	Initial Charge
SOC	State of Charge
$Q_{(battery)}$	Battery Charge

Contents

List of Figures

List of Tables

1
Introduction

This chapter presents the section levels that can be used in the template.

1.1 Background

Conventional fossil fuels Mobility options have always been contributing towards pollution and environmental impacts for about a century. According to the European Environmental Agency(EEA) about 25% of the total greenhouse emission is caused due to the transportation sector[1]. The contribution of different transportation systems have been shown in Figure 1.1. Therefore the adoption of Electric Vehicles is necessary to drive towards a cleaner Environment. The European Commission's "Fit for 55" initiative targets an ambitious reduction in greenhouse gas (GHG) emissions, aiming to decrease these emissions by 55% by the year 2030, relative to levels recorded in 1990 [3]. Electric Vehicles provide a zero emission advantage while operational as well as provide efficiency of about 90 percent[4]. Electric Vehicles have less moving parts therefore they require less maintenance cost as compared to their engine counterparts[5]. The heart of the electric propulsion system is the electric machine which started its journey with Michael Faraday discovering the electromagnetic rotation in 1821, in simple words he discovered that a current carrying conductor placed in a magnetic field could experience force that tries to rotate it[6]. This discovery and along with the contribution of other scientists like William Sturgeon and Thomas Davenport led to the development of the electric machine that we use today[7]. Electric motors have applications in Energy, household appliances, aerospace, automobile and more, but in this paper we focus on the automotive part. In this sector the electrical machine has several advantages that includes higher efficiencies, environmental friendliness, low operational cost, high torque at low rpm, quiet operation as well as less vibrations as compared to conventional fossil fuel engines.

1.2 Aim and Scope

The purpose of this thesis is to design a cooling circuit capable of preventing excessive heating of the rotor and stator end windings in high-speed applications. The target for the cooling circuit is to get a channel output velocity that can effectively hit the end-winding and cover the maximum surface area of the end-winding for better cooling, keeping the pressure difference within the pump limits. To achieve

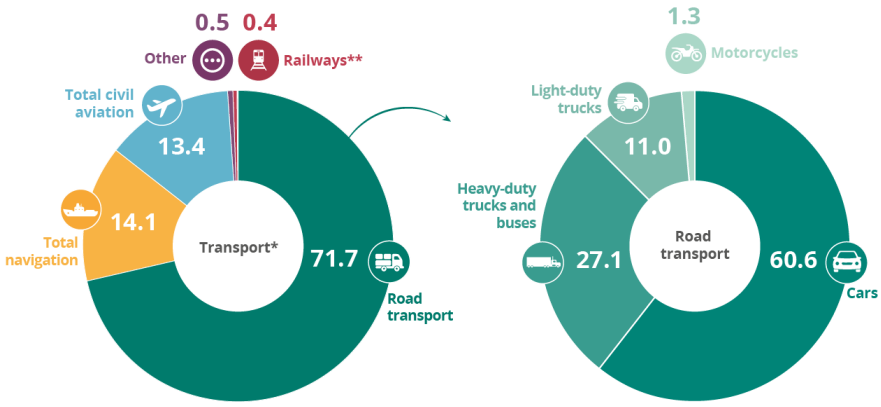

Figure 1.1: Greenhouse gas emissions from transport in the EU[2]

the project's objectives, detailed calculations were conducted to determine the necessary flow rate, pressure, and velocity within the channel, along with the trajectory of the coolant. Subsequently, multiple designs were developed using SolidWorks and SpaceClaim, taking into account various parameters. Computational Fluid Dynamics (CFD) simulations were then performed to ensure the attainment of the required outlet velocity, flow rate, and pressure drop. To align with the cooling design parameters, calculations for the pump head were conducted to identify the suitable pump for the cooling circuit. Once the cooling circuit was finalized, a housing was designed to withstand the high mechanical stresses associated with high-speed applications, while also facilitating easy maintenance.

2
Theory

2.1 Permanent Magnet Synchronous Machine(PMSM)

Numerous automobile manufacturers select motors based on their specific needs, with the Permanent Magnet Synchronous Machine (PMSM) being a favored choice due to its compact dimensions, high efficiency, and superior performance [8]. The concept of utilizing PMSM in automotive applications is well-established; however, recent improvements in magnet materials, such as neodymium-iron-boron (NdFeB), have enabled the creation of even more efficient and powerful motors in smaller packages [9]. This machine features permanent magnets affixed to its rotor core, creating multiple pole pairs for the rotor. The incorporation of these magnets negates the need for brushes or commutators, resulting in silent operation, reduced maintenance, minimized mechanical losses, and a higher power-to-weight ratio compared to brushed motors. The magnets in the rotor generate a magnetic field that interacts with the stator's rotating magnetic field, causing the rotor to rotate in synchronization with it [10]. Such machines are widely used in electric and hybrid vehicles, robotics, and renewable energy systems. While magnets offer numerous benefits, they also present several challenges. The magnets employ rare-earth materials like neodymium, which can be costly and whose availability is influenced by geopolitical, economic, and regulatory factors. Materials such as NdFeB, despite constituting roughly 5% of the motor's components, may account for about 25% of its greenhouse gas emissions. This impact varies with the design and use of the magnets. Furthermore, the cost per kilogram of NdFeB exceeds that of copper and steel combined [11]. The extraction of these materials is environmentally detrimental and often involves unethical labor practices [12]. Additionally, magnets are sensitive to temperature and may demagnetize under high temperatures, particularly in conditions of heavy load or high speed, necessitating robust thermal management systems [13]. The control of machines for variable speed applications becomes more complex, as the magnetic fields of the magnets are immutable. Moreover, managing these high-power magnets during manufacturing and assembly phases poses significant challenges [14].

2.2 Electrically Excited Synchronous Machine(EESM)

An alternative approach involves exciting the rotor with an external DC source, eliminating the need for a mechanical connection. This method entails installing electromagnets instead of permanent magnets in the rotor, which are then powered

by an external current to generate a magnetic field. The motor's speed and torque can be precisely controlled by varying the current supplied to these electromagnets. This adjustment alters the magnetic field strength of the rotor, thereby influencing the interaction between the rotor and stator's magnetic fields [15]. This functionality enables the Electrically Excited Synchronous Motor (EESM) to achieve high efficiency across a broad spectrum of speeds and deliver high torque at low speeds, while its robust design, devoid of magnets, eliminates the risk of demagnetization [16]. Unlike other designs, the EESM does not require the generation of negative d-axis current in the field weakening region; it can merely reduce the current amplitude. This feature makes the EESM a compelling choice for high-speed applications [17]. High-speed applications present several challenges, including the need for a mechanical design robust enough to withstand the significant centrifugal forces encountered at high speeds[18], along with managing the heat generated from copper, iron, and mechanical losses. Copper losses, which arise from the resistance in the copper windings, can be represented by the formula I^2R . At high load conditions, the current through the rotor and stator windings increases substantially, leading to heightened copper [19]. Iron losses in the Electrically Excited Synchronous Motor (EESM) result from hysteresis and eddy current losses. Hysteresis loss occurs due to the core's repeated magnetization and demagnetization, while eddy current losses are induced by circulating currents within the core as the magnetic field changes. These losses increase with the magnetic flux density, especially under high load conditions, thereby elevating heat loss [20] . Additionally, mechanical losses, such as friction in bearings and other moving parts at high velocities, contribute to heating. These factors underline the necessity for an enhanced cooling system in EESM, particularly for high-speed applications. In high-speed applications, selecting the appropriate material for rotor lamination is crucial. The chosen material must exhibit high tensile strength to withstand the substantial centrifugal forces encountered [21]. Additionally, it should possess high fatigue strength to manage the cyclic stress resulting from fluctuating magnetic fields [22]. Effective heat dissipation is essential, necessitating a material with high thermal conductivity to mitigate the heat generated by electrical and mechanical losses. Preference is given to materials with a low coefficient of thermal expansion (CTE), as they exhibit minimal dimensional changes when subjected to temperature fluctuations. Furthermore, a high elastic modulus (stiffness) is desirable to ensure the rotor maintains its shape under the dual pressures of centrifugal and magnetic forces, minimizing the risk of deformation[23]. Such deformation could lead to imbalances and vibrations during operation, underscoring the importance of these material properties.

2.2.1 Stator

The stator is a crucial component in an Electrically Excited Synchronous Machine (EESM), primarily responsible for generating the magnetic field necessary for the operation of the machine. It consists of a cylindrical frame and a series of electrical windings. These windings, when energized by an external power source, produce a magnetic field that interacts with the rotor to produce torque and rotation. The stator's design and functionality are vital for the efficient transformation of electrical

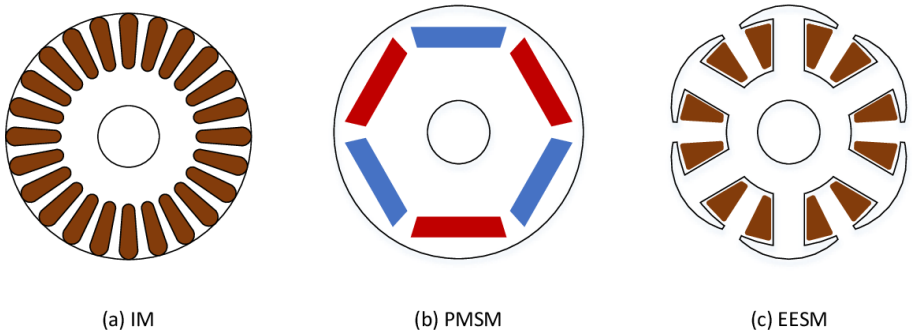

Figure 2.1: Rotor Design of (a)Induction Machine.(b)Permanent Magnet Synchronous Machine(PMSM), (c) Electrically Excited Synchronous Machine.[**?**]

energy into mechanical energy.
The stator cores are typically made up of laminations, thin layers of electrically insulated steel stacked together to reduce eddy current losses. Eddy currents are loops of electrical current induced within conductors by a changing magnetic field in the conductor, according to Faraday's law of induction. These currents within the metal of the stator can generate significant heat and energy losses. By laminating the core, the pathway for these currents is broken up into thinner, less conductive slices, significantly reducing these losses. This lamination helps improve the efficiency of the EESM by minimizing unwanted thermal and energy inefficiencies, thereby enhancing overall performance.

2.2.2 Rotor

The rotor in an Electrically Excited Synchronous Machine (EESM) plays a pivotal role in the electromechanical energy conversion process, central to the operation of the machine. Structurally, the rotor consists of a shaft equipped with magnetic poles, which can be configured using either permanent magnets or electromagnets, depending on the design specifications of the EESM. In the case of electromagnetically excited rotors, the magnetic poles are formed by windings that, when energized, interact with the magnetic field generated by the stator. This interaction produces electromagnetic torque, causing the rotor to rotate and thus converting the electrical energy supplied to the stator into mechanical energy at the rotor shaft. Electromagnetically excited rotors in EESMs utilize laminated steel cores to minimize eddy current losses, enhancing efficiency and performance. This construction reduces heat and energy dissipation, ensuring optimal operational control and efficiency. The careful design of these laminations is crucial for the machine's overall performance.

2.2.3 Windings

In Electrically Excited Synchronous Machines (EESM), windings play a crucial role in the machine's functionality by facilitating the electromechanical energy conversion process. These windings, typically made of copper wire, are wound around the core of both the stator and rotor. In the stator, windings are energized to create a

rotating magnetic field, which in turn induces torque in the rotor. For the rotor, windings may either be excited by a separate DC source or via slip rings and brushes, depending on the machine design.
The configuration and design of these windings determine the machine's electrical characteristics, such as its torque capabilities, efficiency, and operational stability. Properly designed windings optimize the magnetic field distribution within the machine, enhancing performance and reducing losses due to electrical resistance and magnetic saturation. Additionally, the insulation and thermal management of windings are vital to prevent overheating and ensure long-term reliability and safety in operation. Hence, the design, material selection, and implementation of windings are critical aspects that significantly influence the overall performance and efficiency of EESMs.

2.2.4 Housing

In Electrically Excited Synchronous Machines (EESM), the housing is crucial for ensuring structural integrity and operational efficiency. Our design utilizes an aluminum housing, chosen for its strength-to-weight ratio and high thermal conductivity. This material not only robustly protects the internal components from environmental factors but also facilitates efficient heat management.
A distinctive feature of our design is the integration of a cooling fluid inlet directly into the casing, allowing for effective heat transfer. Upon entering through this inlet, the cooling fluid flows into a network of channels embedded within the stator core. This channel network is strategically designed to maximize surface area contact with the stator, enhancing the heat absorption from the core components. The aluminum's thermal properties expedite the heat dissipation process, ensuring that the cooling fluid effectively lowers temperatures throughout the machine. This efficient cooling system is vital for maintaining optimal operational temperatures, preventing overheating, and thereby safeguarding the EESM's longevity and reliability, while sustaining high performance and efficiency.

2.2.5 Copper Loss

Copper Loss in EESM takes place in two ways Copper DC and Copper AC loss. Copper DC loss, technically known as I^2R loss, represents the thermal energy dissipated due to the inherent electrical resistance of the copper windings within the stator and rotor of Electrically Excited Synchronous Machines (EESM). This phenomenon occurs when electrical current traverses the conductor material (copper), encountering resistance that converts a portion of the electrical energy into heat. The magnitude of copper loss is quantitatively expressed by the formula $P = I^2R$, where 'P' denotes the power lost as heat, 'I' indicates the current, and 'R' symbolizes the resistance of the copper windings. These losses are pivotal in determining the thermal and efficiency characteristics of EESM, as excessive heat generation can lead to reduced operational efficiency and potential damage to the machine's components.
Copper AC loss is caused due to skin effect and proximity effect in the stator and

end winding. The skin effect occurs when alternating current (AC) flows through a conductor. Due to electromagnetic induction, the AC creates a changing magnetic field around the conductor. This changing field generates circulating eddy currents within the conductor itself, which oppose the main current. The current tends to concentrate near the surface of the conductor (the skin), rather than being uniformly distributed across its cross-section. In the active winding of an EESM, the current is alternating (AC), and it flows through the stator winding that are directly interacting with the machine's rotating magnetic field. This leads to a strong skin effect because the winding experiences the full impact of the machine's alternating magnetic field. This alternating field is responsible for generating torque and is constantly changing in direction and intensity, which makes the skin effect more pronounced in the active part. The proximity effect arises when conductors are placed close to each other, which is common in stator winding. When AC flows through these conductors, each one generates its own magnetic field. These magnetic fields interact with the nearby conductors, inducing circulating currents within them. As a result, the current distribution within each conductor is distorted, often concentrating the current on one side of the conductor, near the adjacent wire. This distortion increases the effective resistance of the conductor, leading to additional losses.
In the active winding, both the skin effect and proximity effect are strong because the winding experiences a high-intensity alternating magnetic field, which distorts the current distribution and increases resistance. This leads to significant Copper AC losses.
In the end winding, these effects are much weaker because the winding is outside the main magnetic field. The reduced exposure to alternating fields means that skin effect and proximity effect cause only minor losses, hence the assumption of around 20% of the Copper AC losses compared to the active winding was considered.
The higher the frequency of the AC, the more pronounced the skin effect becomes, causing the current to flow closer to the surface and leaving the center of the conductor with little to no current.
Importantly , the resistance 'R' for copper DC loss is not a constant value but varies with temperature according to the below relationship

$$R = R_0(1 + \alpha(T - T_0)) \tag{2.1}$$

where R_0 is the resistance at a reference temperature T_0, T is the operating temperature, and α is the temperature coefficient of resistance for copper. This temperature dependence implies that as the machine operates and heats up, the resistance of the copper windings increases, leading to greater copper losses. Additionally, copper loss is also influenced by the number of phases in the machine. In a multi-phase EESM, the total copper loss is the sum of the losses in each phase. Typically represented in a three-phase system as,

$$P_{\text{total}} = 3I^2R \tag{2.2}$$

This formula underscores that each phase contributes to the overall heat generation, impacting the machine's thermal management and efficiency.
Effective management of copper losses is therefore essential for enhancing the performance and longevity of EESMs.

2.2.6 Iron Loss

Iron loss, also known as core loss, in Electrically Excited Synchronous Machines (EESM) encompasses the energy dissipated due to the magnetic properties of the iron used in the machine's stator and rotor cores. It comprises two main components: hysteresis loss and eddy current loss.
Hysteresis loss occurs due to the lagging of magnetic induction behind the magnetizing force as the magnetic field in the core alternates, causing molecules in the iron core to realign with each changing cycle. This loss is dependent on the material properties of the core, the frequency of the magnetic reversals, and the maximum flux density. It is mathematically described by the Steinmetz equation,

$$P_h = \eta B_{\max}^{\alpha} f \tag{2.3}$$

where η is the hysteresis coefficient, $B_{\max}$ is the maximum flux density, α is the Steinmetz constant (usually ranging between 1.5 and 2.5), and f is the frequency of magnetic field reversals.
Eddy current loss results from circulating currents induced within the core material due to the changing magnetic field. These currents create their own magnetic fields which oppose the original field, leading to energy dissipation in the form of heat. The power loss from eddy currents can be expressed as

$$P_e = K_e (B_{\max})^2 t^2 f^2 \tag{2.4}$$

, where K_e is the eddy current coefficient, t is the thickness of the lamination, and f is the frequency.
The total iron loss is thus the sum of hysteresis and eddy current losses, each influenced by factors like frequency, core material, core geometry, and lamination thickness. Managing these losses is critical for the efficiency and thermal performance of EESM.
Effective control and reduction of iron losses are vital for enhancing the operational efficiency and durability of EESMs, making them a focal point in the design and operation of these machines.

2.3 Fluid Mechanics

The concept of fluid mechanics and the equations associated with it are necessary for thorough understanding of CFD simulations. The primary equations governing these simulations are derived from the conservation laws of physics specifically, conservation of mass, momentum, and energy.

2.3.1 Continuity Equation

The continuity equation is fundamental in fluid dynamics to ensure mass conservation in fluid flow, especially significant in incompressible flow analysis:

$$u = 0 \tag{2.5}$$

This vector equation states that the divergence of the velocity field u is zero, implying that the mass flow into any control volume is equal to the mass flow out, signifying mass conservation.

2.3.2 Momentum Equation

The momentum equations, often referred to as the Navier-Stokes equations for viscous flows, describe the force balance on a fluid particle:

$$\rho\left(\frac{\partial u}{\partial t} + u \cdot \nabla u\right) = -\nabla p + \mu\nabla^2 u + f \tag{2.6}$$

Here, ρ is the fluid density, u is the velocity vector, p is the pressure, μ is the dynamic viscosity, and f represents body forces (e.g., gravity). In steady-state simulations, the time derivative term $\frac{\partial u}{\partial t}$ is zero, simplifying the equation to only include convective and viscous forces, along with any external forces.

2.3.3 Energy Equation

The energy equation is used to determine temperature distribution within the flow and is particularly relevant for flows where heat transfer is involved:

$$\rho c_p\left(\frac{\partial T}{\partial t} + u \cdot \nabla T\right) = \nabla \cdot (k\nabla T) + \Phi \tag{2.7}$$

In this equation, T is the temperature, c_p is the specific heat at constant pressure, k is the thermal conductivity, and Φ represents heat generated by viscous dissipation. For steady-state analysis, the time-dependent term is eliminated.

2.3.4 Bernoulli's Equation

Bernoulli's Equation is a fundamental principle in fluid dynamics that describes the behavior of a fluid moving along a streamline. This equation is derived from the conservation of energy principle and states that for an inviscid flow (where viscous forces are negligible), the total mechanical energy of the fluid along a streamline remains constant. Bernoulli's Equation can be expressed as follows:

$$P + \frac{1}{2}\rho v^2 + \rho g h = \text{constant} \tag{2.8}$$

Where P is fluid pressure, ρ is the density of the fluid, v is the velocity of the fluid, g is the acceleration due to gravity and h is the height above a reference level. In the equation each term is associated with a type of energy, the P in the equation symbolizes the potential energy due to pressure of fluid, $\frac{1}{2}\rho v^2$ represents the kinetic energy of the fluid and $\rho g h$ is the potential energy due to the height of the fluid above a reference level.

2.3.5 Reynold Number

In the study of fluid dynamics and heat transfer within the context of computational fluid dynamics (CFD), two dimensionless numbers are particularly crucial, the Reynolds number and the Nusselt number. The Reynolds number (Re) is a dimensionless quantity that helps predict flow patterns in different fluid flow situations. It is defined as the ratio of inertial forces to viscous forces and is given by the formula

$$\mathrm{Re} = \frac{\rho U L}{\mu} \tag{2.9}$$

where ρ is the fluid density, U is the flow velocity, L is the characteristic length, and μ is the dynamic viscosity. It serves as a criterion for determining whether the flow will be laminar or turbulent. Flows with Reynolds number less than 2300 are typically laminar, while Re values greater than 104 indicate turbulent flows.

2.3.6 Nusselt number

Nusselt number (Nu) is a measure of convective heat transfer relative to conductive heat transfer across a boundary. It is expressed as

$$\mathrm{Nu} = \frac{hL}{k} \tag{2.10}$$

where h is the convective heat transfer coefficient, L is the characteristic length, and k is the thermal conductivity. The Nusselt number is essential for analyzing the efficiency of heat transfer processes, allowing for the evaluation and enhancement of equipment design in engineering applications. Together, these numbers play pivotal roles in the characterization and optimization of flow and thermal processes in CFD simulations.

2.4 Heat Transfer

Heat transfer is a critical process in many engineering applications, involving the movement of thermal energy from higher to lower temperature regions. The three primary modes of heat transfer are conduction, convection, and radiation, each characterized by distinct mechanisms and described by specific equations.

2.4.1 Conduction

Conduction is the heat transfer through a material without the movement of the material itself, occurring via molecular or electron motion within the substance. It is quantitatively described by Fourier's Law, which states:

$$q = -k\nabla T \tag{2.11}$$

Where q is the heat flux (amount of heat transferred per unit area per unit time), k is the thermal conductivity of the material (a measure of its ability to conduct heat), and ∇T is the temperature gradient within the material. The negative sign indicates that heat flows from higher to lower temperatures.

2.4.2 Convection

Convection involves the transfer of heat between a solid surface and a moving fluid, depending on the relative motion between the surface and the fluid. The heat transfer in convection is expressed using Newton's Law of Cooling:

$$q = h(T_s - T_f) \tag{2.12}$$

where q is the convective heat flux, h is the convective heat transfer coefficient (which depends on the type of fluid motion and properties of the fluid), T_s is the surface temperature, and T_f is the fluid temperature far from the surface. Furthermore, convection can be classified into two types, natural and forced convection. Natural convection, where fluid motion is caused by buoyancy forces that result from density variations due to temperature differences within the fluid. Forced convection, where fluid motion is induced by external means, such as fans or pumps.

2.4.3 Radiation

Radiation is the transfer of energy by electromagnetic waves and can occur through a vacuum. All bodies emit, absorb, and transmit radiation, depending on their temperature and surface properties. The amount of energy radiated by a body is given by the Stefan-Boltzmann Law:

$$q = \epsilon \sigma T^4 \tag{2.13}$$

where q is the heat emitted per unit area, ϵ is the emissivity of the material (a measure of a material's ability to emit energy as radiation), σ is the Stefan-Boltzmann constant and T is the absolute temperature of the body.

2.5 Computational Fluid Dynamics

Computational Fluid Dynamics (CFD) is a crucial simulation tool for analyzing fluid flow and associated phenomena, using advanced numerical methods to overcome the limitations of traditional experimental approaches. In my thesis, the k-epsilon turbulence model was adopted, a widely-used method for handling turbulent flow due to its robustness and accuracy across a range of flows. This model uses two equations to resolve the turbulent kinetic energy (k) and its dissipation rate (epsilon):
Turbulent kinetic energy (k) equation:

$$\frac{\partial(\rho k)}{\partial t} + \frac{\partial(\rho k u_i)}{\partial x_i} = P_k - \rho\epsilon + \frac{\partial}{\partial x_j}\left[\left(\mu + \frac{\mu_t}{\sigma_k}\right)\frac{\partial k}{\partial x_j}\right] \tag{2.14}$$

Dissipation rate (epsilon) equation:

$$\frac{\partial(\rho\epsilon)}{\partial t} + \frac{\partial(\rho\epsilon u_i)}{\partial x_i} = \epsilon k \left(C_1\epsilon P_k - C_2\rho\epsilon\right) + \frac{\partial}{\partial x_j}\left[\left(\mu + \frac{\mu_t}{\sigma_\epsilon}\right)\frac{\partial\epsilon}{\partial x_j}\right]$$

(2.15)

Here, $\rho\epsilon$ represents the production of turbulence kinetic energy, μ_t is the turbulent viscosity, and $C_1\epsilon$, $C_2\epsilon$, σ_k, and σ_ϵ are model constants. The k-epsilon model offers a practical balance between computational efficiency and the ability to accurately predict flow features such as recirculations and pressure drops, making it invaluable for optimizing designs and enhancing performance across diverse applications, including aerospace, automotive, and energy sectors.

3

Methods

In the computational fluid dynamics (CFD) analysis of the cooling model, the simulation was segmented into two distinct phases Figure 3.1. The first phase focused on the fluid dynamics within the channels embedded in the stator core. Given that the fluid behavior in these channels exhibits minimal temporal variation, it was deemed appropriate to employ a steady-state simulation. This approach not only aligns with the expected physical phenomena but also offers significant savings in terms of computational resources and time.

The second phase of the simulation addressed the fluid dynamics as the coolant exits the stator channels and interacts with the end windings. Unlike the first phase, the fluid behavior in this region is highly transient, characterized by complex interactions with air and the physical structures of the end windings. As the coolant emerges from the outlet, its trajectory and subsequent impact on various sections of the end windings necessitate a transient simulation to accurately capture the dynamic behavior and transient thermal effects within this part of the cooling system. This methodological division ensures that each segment of the model is analyzed under the most appropriate computational approach, enhancing both the efficiency and accuracy of the simulation results.

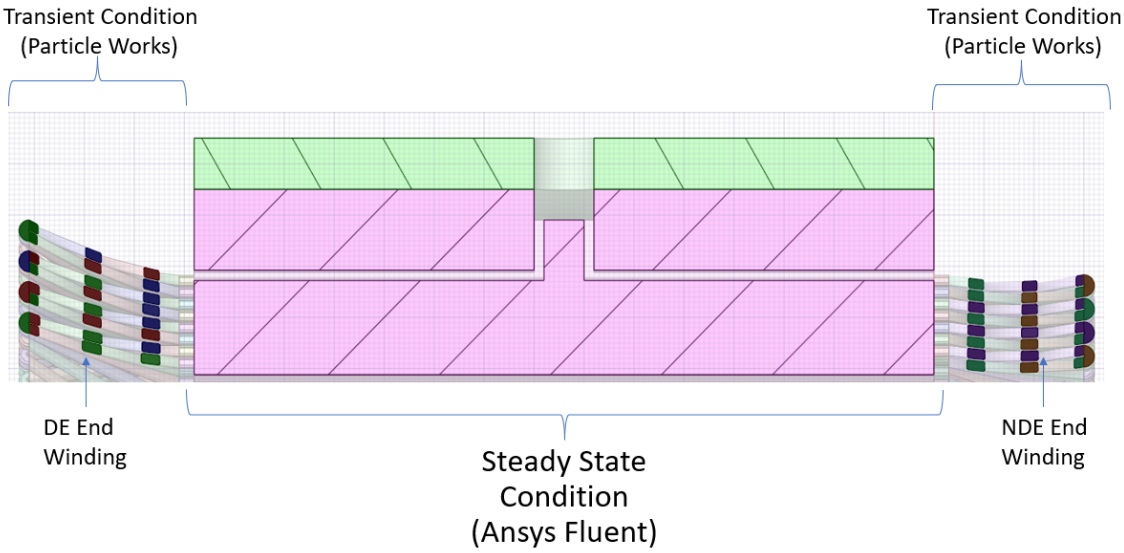

Figure 3.1: Regions for Steady State and Transient Simulation

3.1 Steady State CFD Simulation

In contrast to transient simulations which require time-dependent calculations to observe fluid behavior, steady-state simulations assume that fluid properties remain constant over time. This is advantageous in scenarios where flow conditions are stable or the interest lies in the final equilibrium state. In Ansys Fluent, conducting a steady-state simulation involves a series of straightforward steps designed to accurately represent static conditions, simplifying the computational process and focusing on the equilibrium outcomes Figure 3.2.

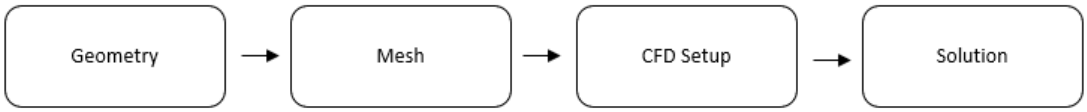

Figure 3.2: Methodology for Steady State CFD Simulation

3.1.1 Geometry

The initial phase of the project involved designing the geometry of the cooling channels within the stator core, utilizing SolidWorks software. This design served as the foundational model in an iterative process aimed at achieving the most optimal configuration. Initially, the cooling channels were conceptualized with minimal constraints to establish a reference design. Subsequent simulation results informed a series of design modifications to accommodate practical constraints and desired outcomes.
Adjustments to the design parameters were made incrementally, based on iterative simulation feedback, to converge on the final design. An essential aspect of the design process was ensuring manufacturability and cost-efficiency. This was addressed by minimizing the number of laminations required for the stator core to reduce production costs. Additionally, the dimensions of the channels were carefully chosen to facilitate manufacturability, and material usage was optimized to minimize waste. Each step of the design refinement was strategically implemented to balance performance, cost, and manufacturability.
The subsequent step involved preparing the geometry for the simulation, which was executed using ANSYS SpaceClaim. In this stage, the specific volume through which the coolant would flow was delineated Figure 3.3. The process included identifying and specifying the inlet and outlet faces of the geometry, setting the stage for detailed CFD simulation. This preparation ensured that the simulation environment was accurately structured to reflect the real-world fluid dynamics scenario.

3.1.2 Mesh

In my research, the model was imported into ANSYS Fluent Meshing for mesh generation. This software notably automates several meshing steps, such as local sizing adjustments, detection of inlets and outlets, boundary layer addition, and

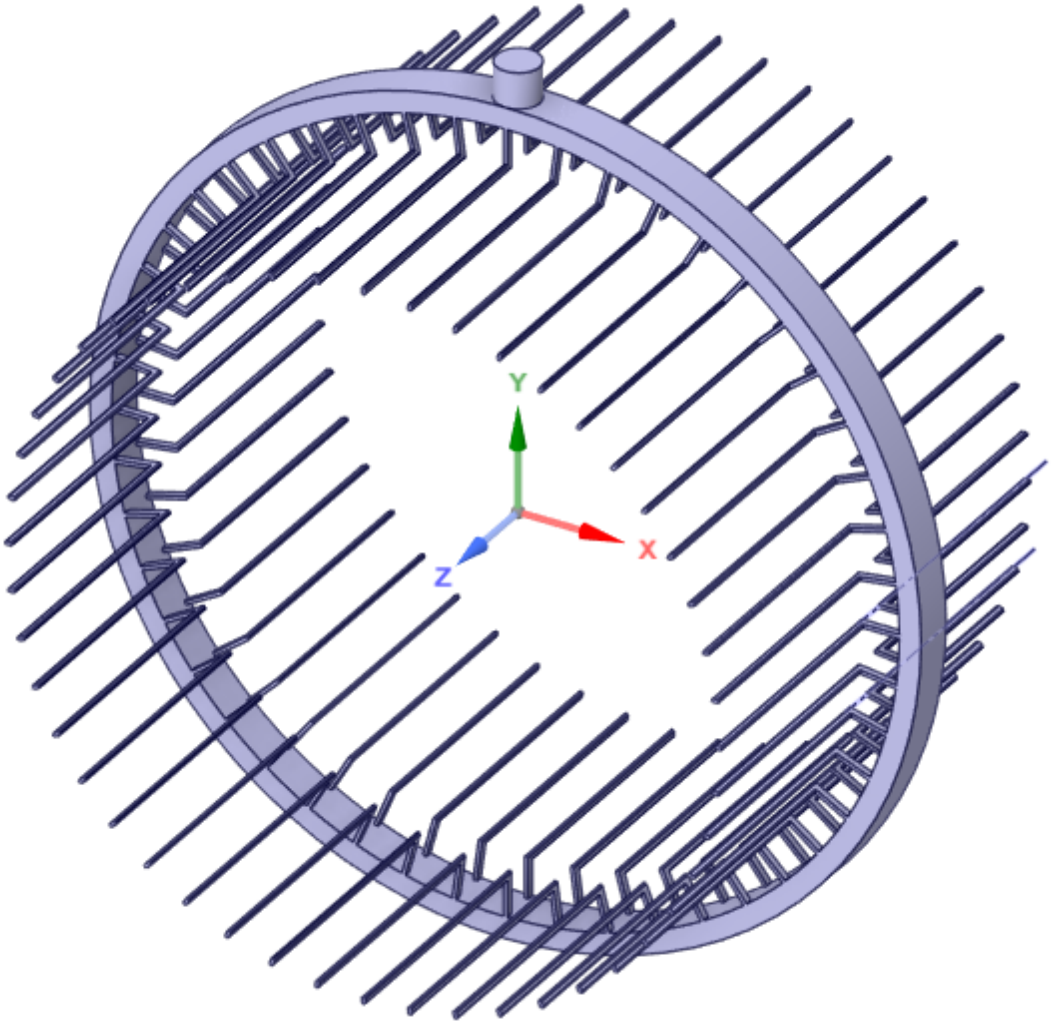

Figure 3.3: Fluid Region of Cooling System

volume mesh creation. Despite its automation capabilities, user intervention is still required to specify certain parameters.

For this study, a 'Watertight Geometry' was selected during import. This term refers to a 3D geometry that is completely enclosed without any gaps or holes, which is crucial for generating an efficient mesh conducive to accurate simulations. Given the simplicity of the model, local sizing was deemed unnecessary, as the standard mesh settings provided satisfactory results.

The quality of the surface mesh was quantified by a skewness factor, with a target value of 0.6 achieved, indicating good mesh quality unlikely to cause computational issues. The geometry setup was straightforward, encompassing only fluid regions without voids, negating the need for multi-zone settings or shared topology.

Automatic detection of boundary types facilitated the identification of regions such as inlets and outlets, although manual adjustments were possible if required. The software also correctly recognized the model as comprising solely fluid regions.

The addition of boundary layers was a critical step, essential for accurately capturing turbulence, viscous effects, and velocity gradients in near-wall regions. The volume mesh was finally generated using a poly-hexcore method, culminating in a mesh structure optimized for the subsequent fluid dynamics simulation Figure 3.4. This comprehensive setup ensured the fidelity and reliability of the simulation results, pivotal for the analytical objectives of this thesis.

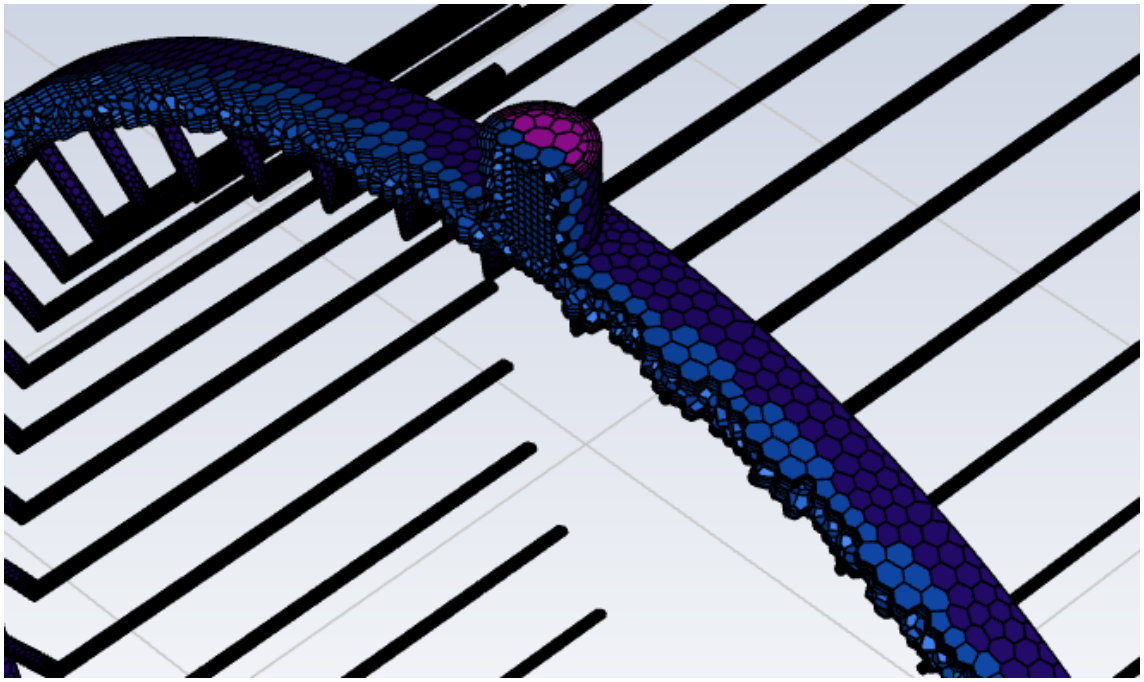

Figure 3.4: Volume Mesh Section

3.1.3 CFD Setup

The next step involves setting up the model using our study conditions. This involves selecting the appropriate type of simulation such as transient model or steady state model etc. In this study steady state study was selected. There are options to select models or equations we want to use, for this case k-omega model was selected, this was due to its good predictions in near wall regions, its less sensitivity for free stream conditions and its robustness in adverse pressure gradients. Furthermore, the materials properties used in this study were defined including the coolant properties at 65 deg C. The cell zone for the model was kept as fluid, as only the volume involving the coolant flow was extracted. Then in the boundary conditions, the inlet velocity was given as 1.618 m/s, which was calculated using the pump flow rate to the machine. The SIMPLE (Semi-Implicit Method for Pressure Linked Equations) was used for the simulation as it offers efficient handling of incompressible flows, stability and robust handling of pressure-velocity coupling.

3.1.4 Solution

This is the final step where we observe the results obtained. Inlet pressure and outlet velocity are the main variables that are observed. In case of outlet velocity, it is important to look for per outlet average velocity and not just the average velocity combined of all outlets. Another thing to consider is to check if the per outlet average outlet velocity reached the target being set by the projectile calculation.

3.2 Modeling of Cooling Channels

This chapter outlines the methodology employed to design the cooling circuit for the Electrically Excited Synchronous Machine (EESM) Figure 3.5. Initially, a preliminary stator core design was established using Ansys Maxwell, based on achieving the requisite electromagnetic performance targets. Subsequently, endwinding models for both the driver-end (DE) and non-driver-end (NDE) were developed in Ansys Spaceclaim, utilizing drafting dimensions provided by the manufacturer. The third phase involved calculating the projectile motion of coolant particles to ensure targeted cooling of the end windings. This analysis determined the necessary target pressure drop and outlet velocity from the cooling channels. A parameter-driven design approach was then applied to create various channel configurations within the stator core, which were iteratively simulated in Ansys Fluent to refine the design. Upon finalizing the design, a 3-D printed model was constructed to empirically validate the coolant flow simulations, ensuring the design met its intended specifications.

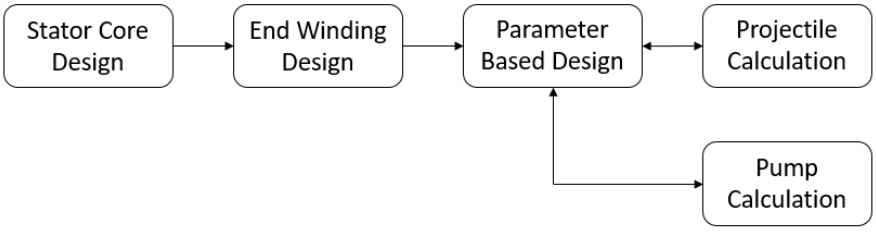

Figure 3.5: Methodology for Modeling of Cooling Channels

3.2.1 Stator Core Design

Designing a stator in Ansys Maxwell involves a systematic approach that integrates electromagnetic theory with practical engineering constraints to optimize performance, efficiency, and manufacturability Figure 3.6. The initial step involves defining the geometric parameters such as the outer and inner diameters, core length, and slot dimensions. This is followed by specifying the electrical parameters including the number of slots, slot pitch, type of windings, turns per coil, and wire gauge. Material properties for both the core and the windings need to be selected based on their magnetic and electrical characteristics.
The design process in Ansys Maxwell utilizes finite element analysis (FEA) to simulate and analyze the electromagnetic behavior of the stator. The simulation helps in

assessing magnetic flux distribution, core losses, and electromagnetic forces, providing insights into how changes in design variables affect performance. The software's parametric and optimization tools are leveraged to fine-tune the design parameters, aiming to minimize losses and maximize efficiency.
Throughout the design iteration, particular attention is paid to the effects of harmonics on the magnetic and electric loading to ensure that the machine will operate efficiently under various loading conditions.

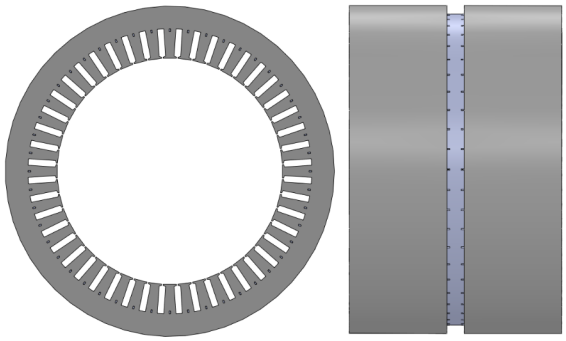

Figure 3.6: Stator Core Design

3.2.2 End Winding Design

End Windings in electric machines are crucial for connecting coil turns or phases beyond the stator or rotor core, forming loop connections between successive coil turns and phases. Their design is pivotal in affecting electromagnetic fields, cooling efficiency, and mechanical stability. In this project, detailed drafting specifications for both the driver-end (DE) and non-driver-end (NDE) end windings were supplied by the manufacturer. Utilizing these specifications, the Computer-Aided Design (CAD) of the end windings was meticulously executed in SolidWorks, adhering closely to the provided dimensions Figure 3.7. Subsequently, the designed end windings were accurately assembled with the stator core and housing, ensuring a precise integration of components within the overall machine assembly. This process was critical in achieving optimal alignment and functionality of the electrically excited synchronous machine.

3.2.3 Projectile Calculation

To optimize the cooling of the end winding in the electrically excited synchronous machine, precise targeting of coolant drop was critical. By employing kinematic equations of motion, the trajectory of coolant per second was calculated, allowing for an accurate estimation of the necessary outlet velocity from the cooling channels. This calculated velocity aimed to ensure the droplets reached the midpoint of the end winding, which was determined as the optimal target region to enhance coverage and efficiency. The ability to approximate the target outlet velocity from these initial calculations gave a target that design had to meet for proper cooling of the end

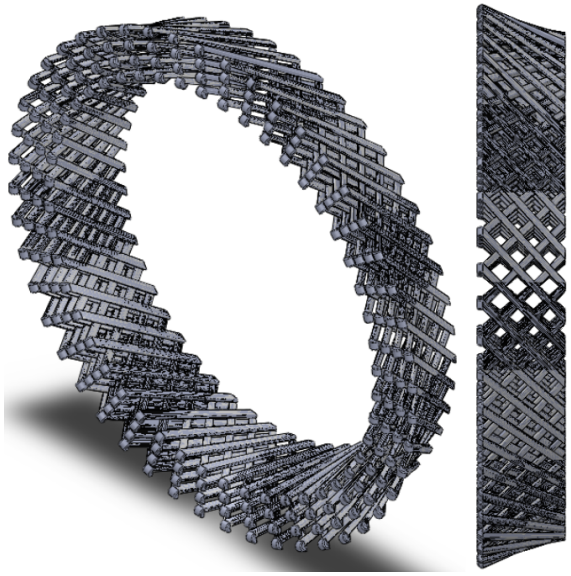

Figure 3.7: DE Endwinding Design

winding. This strategic approach streamlined the development process, provided direction and expediting the achievement of desired thermal management objectives in the machine design.
Taking flow rate as Q_{lm}, that is the amount of fluid flowing(Liters) from a cross section for every minute.

$$Q_{\text{ms}} = \frac{Q_{\text{lm}} \times 10^{-3}}{60} \tag{3.1}$$

$$V_{\text{ts}} = \frac{Q_{\text{ms}}}{N_s} \tag{3.2}$$

Where Q_{ms} is the amount of fluid flowing(m3) from a cross section for every second, V_{ts} is the total volume of fluid flowing from a single slot (m3) per second. N_s is the number of slots in the machine.
From kinematic equations of motion in Y direction,

$$s = ut + \frac{1}{2}gt^2 \tag{3.3}$$

Where s is the height of the slot in Y direction in m/s, u is initial velocity of the fluid in Y direction in m/s, g is acceleration due to gravity and t is time taken to reach s distance.

$$t = \sqrt{\frac{S_y}{2g}} \tag{3.4}$$

Velocity in X direction can be written as,

$$v_x = \frac{S_x}{t} \tag{3.5}$$

Flow rate Q_{lm} of the coolant entering the inlet from the housing is 12 Liters per minute(Lpm) and the density of the coolant at 60°C. Using the above equations, v_x of fluid comes out to be 0.9899 m/s (Appendix A).

3.2.4 Pump Height Calculation

Pump height, often referred to as total dynamic head in hydraulic systems, is a critical parameter for ensuring the efficient operation of a pumping system. Figure 3.8 illustrates the coolant flow path within the machine. The coolant enters the system through the inlet located in the casing, proceeds through the designated channels, and strikes the end windings to provide cooling. Afterward, it is collected in a reservoir and directed to the pump, which recirculates the coolant back to the inlet, maintaining a continuous cooling cycle. It represents the total height that a pump must lift a fluid, combining the static lift, the height the fluid must be elevated, and the resistance due to friction and other components in the system like valves and bends.
The total dynamic head TDH can be calculated using the following equation:

$$\text{TDH} = \text{Pressure Head}(H_p) + \text{Friction Head}(H_f) + \text{Discharge Head}(H_d) \tag{3.6}$$

Pressure head is the head required by the pump to overcome the pressure difference

$$H_p = \frac{\Delta P}{\rho g} \tag{3.7}$$

H_p is the head required to overcome the pressure difference between the inlet and the outlet of the pump, ΔP is the pressure difference (in Pascals), ρ is the density of the fluid (in kg/m^3), g is the acceleration due to gravity (approximately 9.81 m/s^2). Friction head losses occur due to the resistance to flow within the pipe and other components like fittings, valves, and bends in the system. These can be calculated using the Darcy-Weisbach equation:

$$H_f = \frac{fLv^2}{2Dg} \tag{3.8}$$

where f is the friction factor (which can depend on the pipe's material and the flow's roughness), L is the length of the pipe, D is the diameter of the pipe, v is the flow velocity, and g is the acceleration due to gravity.
Discharge head is the vertical distance from the pump's discharge or the centerline up to the highest point of the outlet pipe or the discharge point. It essentially measures the elevation the pump needs to overcome to push the fluid to its intended height.

$$H_d = z_2 - z_1 \tag{3.9}$$

For the above mentioned inputs, a pump height of 5.44 m was obtained (Appendix B).

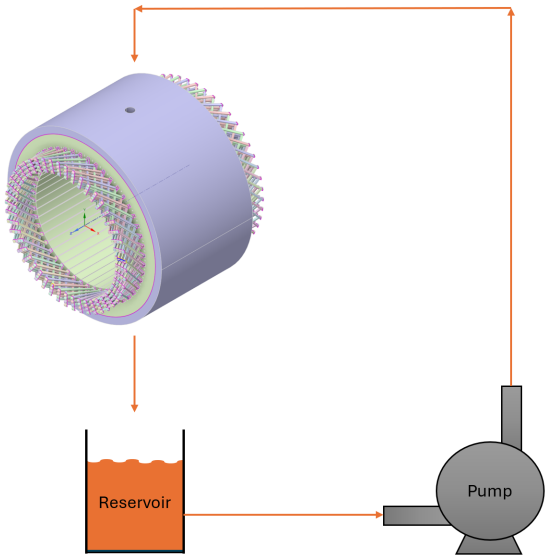

Figure 3.8: Coolant Flow Diagram

Inputs	Value
Diameter of pipe at outlet(D)	0.012 m
Velocity at outlet(v)	1 m/s
Acceleration due to gravity(g)	9.81 m/s^2
Density of coolant(ρ)	804.33 kg/m^3
Friction factor(f)	0.07
Length of Pipe 1	0.030 m
Length of Pipe 2	0.250 m
Fitting factor for bends(k)	0.5
Pressure at outlet	40000 Pa
Pressure at inlet	0 Pa
Height of the outlet(z_2)	0.260 m
Height of the inlet(z_1)	0 m

Table 3.1: Design parameters and their values

3.2.5 Parameter Based Design of Cooling Channels

The primary objective in designing the cooling circuit for the electrically excited synchronous motor (EESM) was to regulate the temperature of both the windings and the stator core to maintain operational efficiency and minimize thermal stress. The stator core is made up of several laminations, reducing eddy current losses, enhancing overall performance. A key goal was to achieve desired coolant velocity and pressure drop at the outlet using the minimal number of lamination types to simplify manufacturing and reduce costs.

In designing the cooling channels, it was crucial to minimize the removal of stator core material to preserve the magnetic flux density and, consequently, the machine's torque. The coolant flow begins at an inlet within the housing Figure 3.9 and Figure 3.10, progresses into a main channel, and then divides into secondary type

2 channels before entering the narrower type 1 channels, ensuring the fluid exits at the target speed. A larger main channel could result in uneven coolant flow distribution, where channels closer to the inlet receive more flow than those farther away, leading to variations in cooling efficiency. Rapid filling of the main channel was essential to establish uniform pressure that drives coolant evenly through all subsidiary channels.
To optimize the cooling of the windings, channel outlets were strategically located near the winding slots. Type 2 channels facilitated the transfer of coolant from the main channel to these outlets, conserving stator material and transforming the coolant's potential energy into kinetic energy, thereby increasing its velocity. Finally, the type 1 channels were designed to ensure a consistent and smooth laminar flow, optimizing the heat transfer from the stator and windings to the coolant. This approach not only enhances the cooling effectiveness but also maintains the structural integrity and performance of the motor.

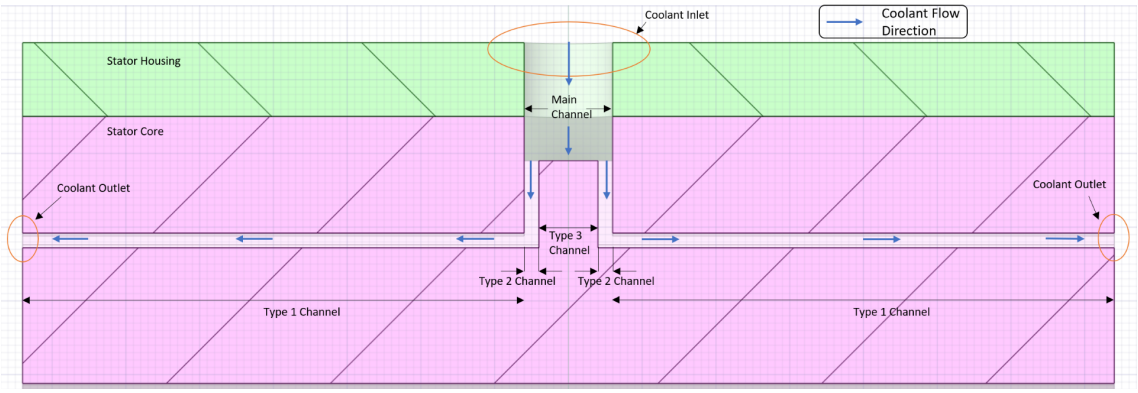

Figure 3.9: Model Design Parameters (a)

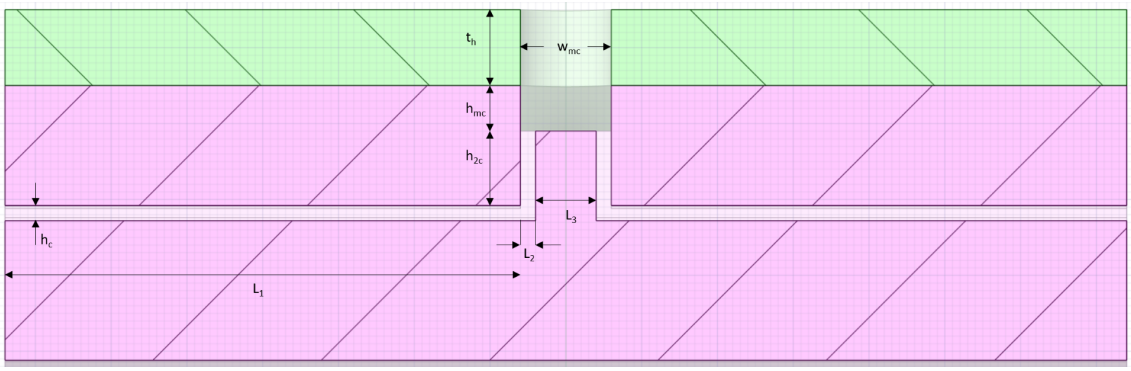

Figure 3.10: Model Design Parameters (b)

3.2.5.1 Design 1

In the optimized design, only two types of laminations are necessary, simplifying manufacturing and reducing costs. The type 1 channels are engineered with a 13 mm height to maximize coverage of the end windings, ensuring uniform cooling across

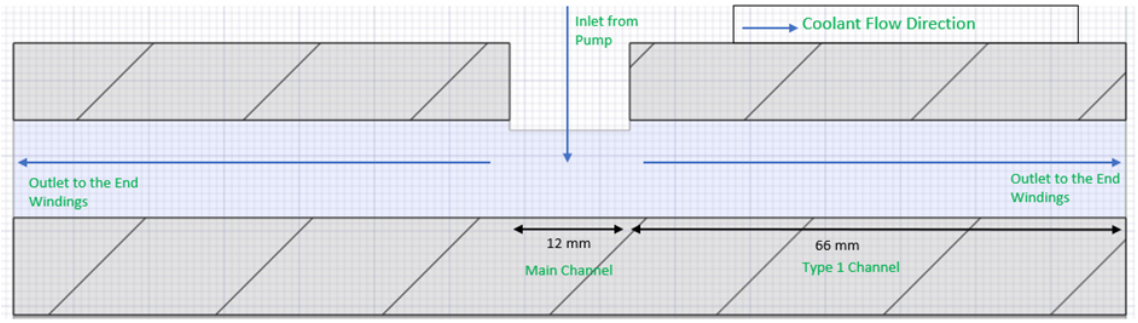

Figure 3.11: Design 1 Channel Cross-Section

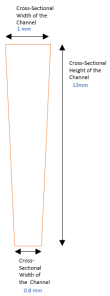

Figure 3.12: Cross Section of Design 1 Outlet Face

this critical component Figure 3.11 . The channel's cross-section is designed as trapezoidal—wider at the top and narrower at the bottom Figure 3.12. Figure 3.13 illustrates the lamination design. The Type 1 lamination, depicted on the left of (Figure 3.13 left) extends from the termination of the main coolant channel to the end of the stator core's active length. This lamination features active winding slots and incorporates 48 trapezoidal channels specifically designed to facilitate coolant flow. The type 2 (Figure 3.13 right) covers the main channel's width and also contains the slots for active winding. This idea was to help maintain a consistent fluid velocity across the outlet cross section, enabling more efficient cooling coverage of the end windings. By adopting this shape, the design counters the effects of gravity that might otherwise cause coolant to concentrate more heavily at the lower part of the outlet, ensuring that the coolant flow is distributed more evenly despite the gravitational pull. Material Utilized = 6.75%
The design was simulated with an 11 L/min coolant flow rate at the inlet from the pump. However, the results indicated that the design failed to achieve the target velocity. An analysis based on Bernoulli's equation reveals that the high volume of the type 1 channel does not create the necessary pressure drop to propel the coolant with sufficient velocity towards the outlet Figure **??**. This insight highlights the need for adjustments in the channel dimensions.

3.2.5.2 Design 2

In this revised design, three types of laminations are utilized Figure 3.18. Previously, insufficient velocity at the outlet prompted a modification: the thickness of the type 2 channel was decreased to narrow its cross-section, thereby increasing the pressure

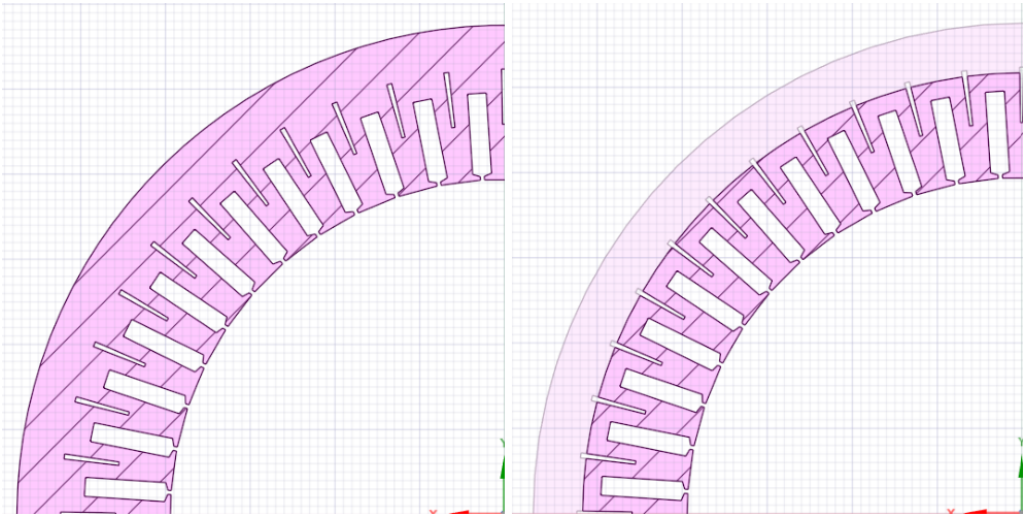

Figure 3.13: Laminations for Design1

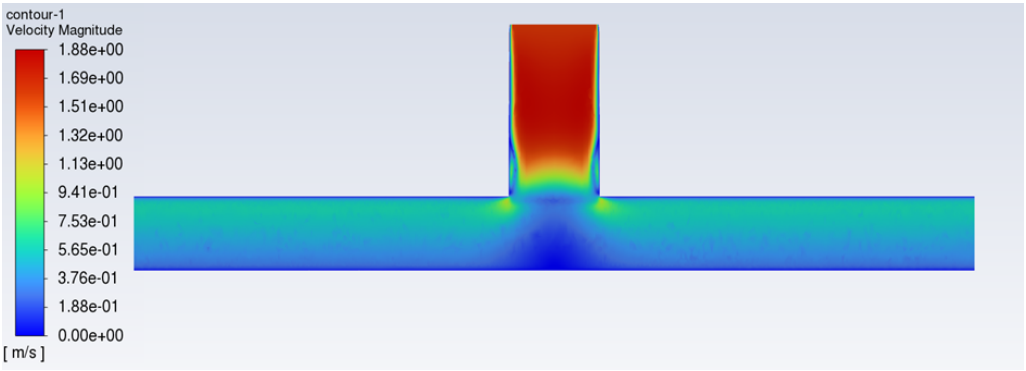

Figure 3.14: Velocity Distribution for Design 1

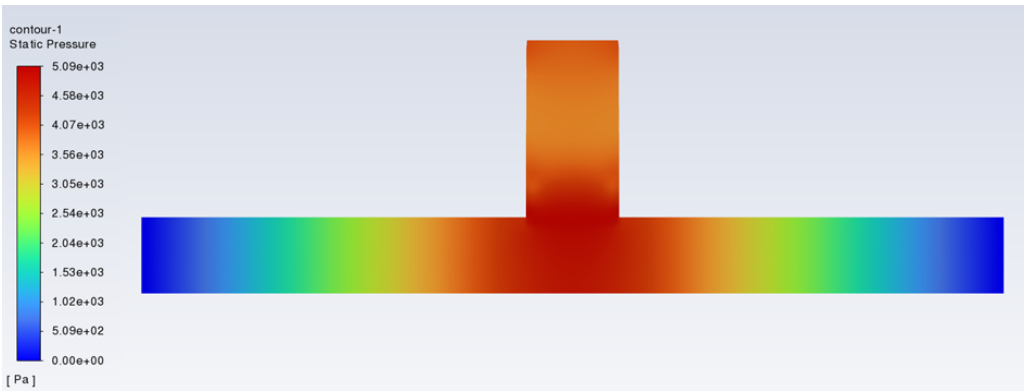

Figure 3.15: Pressure Distribution for Design 1

drop from the main channel and consequently the coolant velocity within the type 2 channel. However, this alteration could result in a jet-type flow from the outlet, which might cover a smaller surface area of the end winding. To mitigate this, a wider type 1 channel was implemented. The larger cross-section of the type 1 channel significantly reduces the pressure, transforming the narrow jet into broader, more

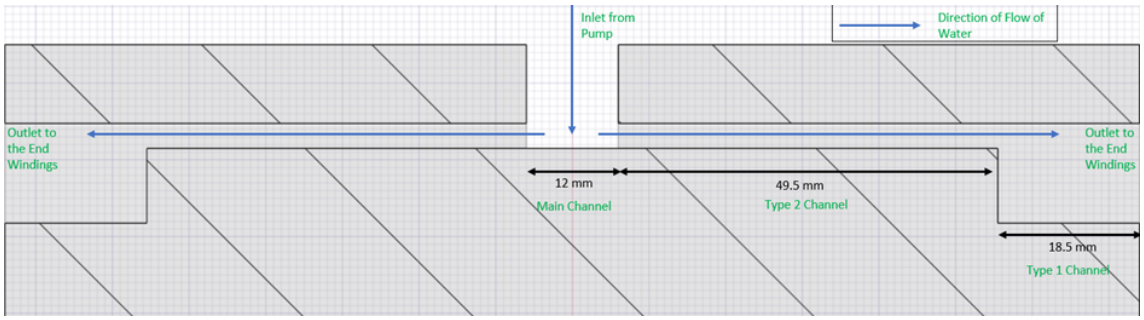

Figure 3.16: Design 2 Channel Cross-Section

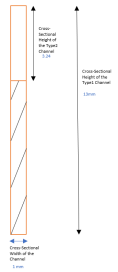

Figure 3.17: Cross Section of Design 2 Outlet Face

dispersed streams of coolant. This design adjustment enhances coverage, ensuring more effective cooling across the maximum surface area of the end winding. Material Utilized is 5.6%.

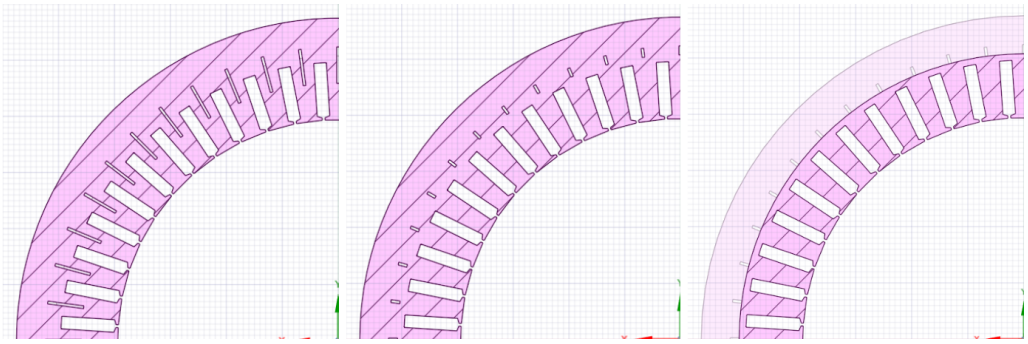

Figure 3.18: Laminations for Design2

In this design iteration, improvements were noted in the average outlet velocity Figure 3.19, and a discernible sprinkling effect was visible in the velocity contours. Despite these enhancements, the average velocity remains below the target, primarily due to the expanded cross-section of the type 1 channel. Also, a non-uniform velocity distribution across the outlet cross-section was observed, with higher velocities observed in the upper regions compared to the lower. Furthermore, this design necessitates the use of three types of laminations, an increase from the two types required in the previous configuration.

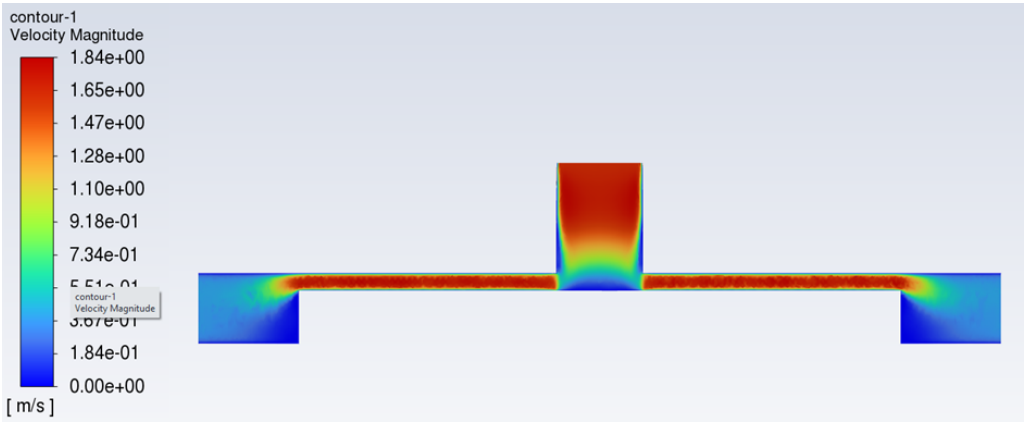

Figure 3.19: Velocity Distribution for Design 2

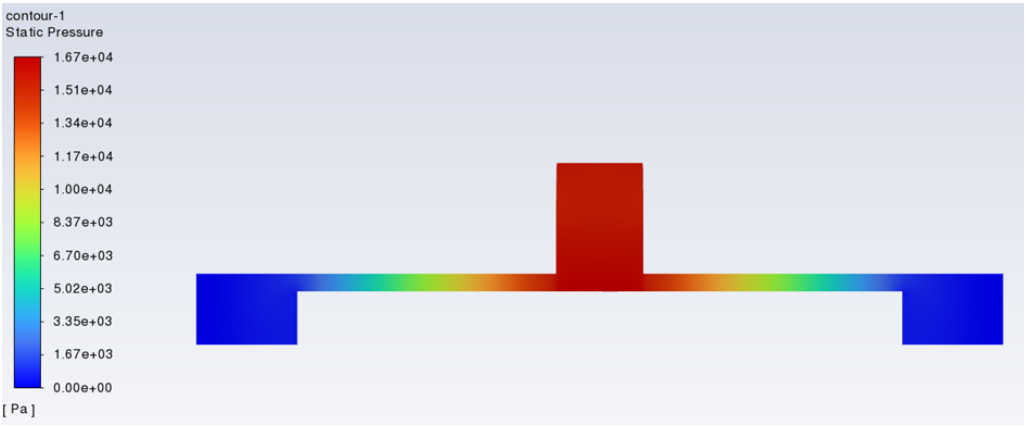

Figure 3.20: Pressure Distribution for Design 2

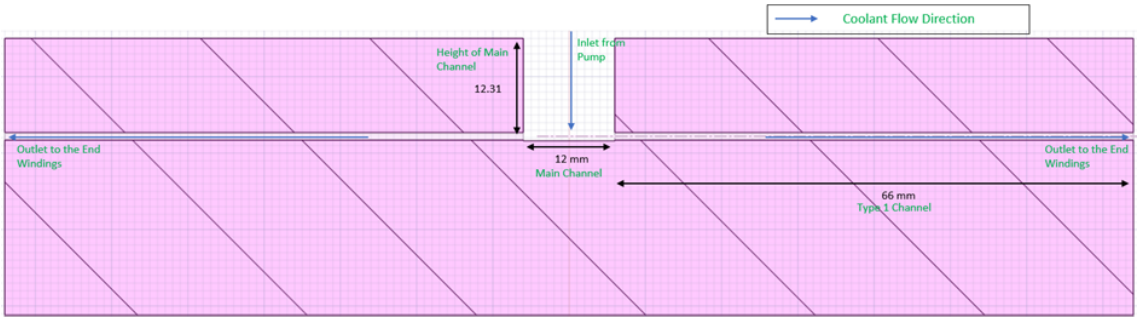

Figure 3.21: Design 3 Channel Cross-Section

Figure 3.22: Cross Section of Design 3 Outlet Face

3.2.5.3 Design 3

In response to the shortcomings of the previous iteration, this design utilizes two types of laminations to construct cooling channels within the stator core Figure 3.21.

The cross-sectional dimensions were minimized to achieve the desired average outlet speed Figure 3.22. Simplification was a key aspect of this design, incorporating type 1 channels with a circular cross-section to reduce the wetted surface area, thereby reducing friction between the fluid and the channel walls. This adjustment facilitates a more symmetrical fluid flow, enhancing cooling efficiency. 3.5%

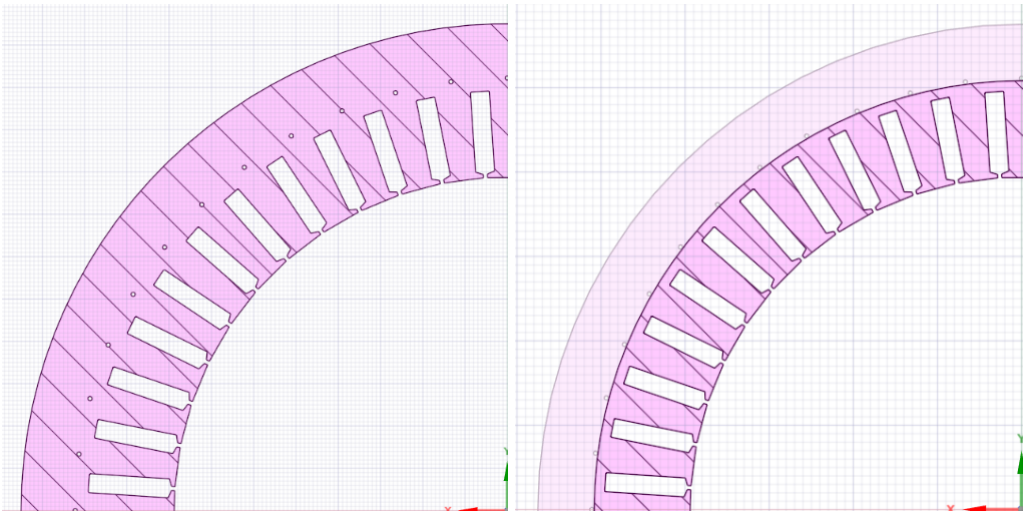

Figure 3.23: Laminations for Design3

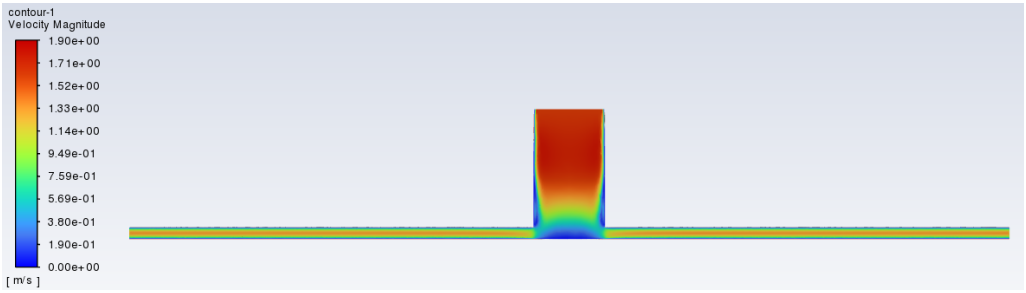

Figure 3.24: Velocity Distribution for Design 3

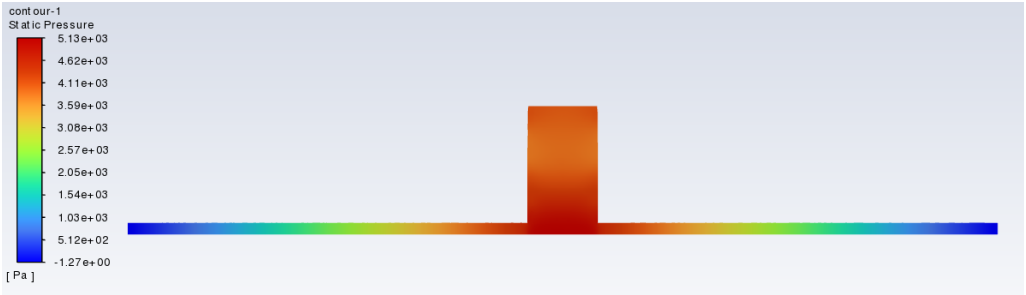

Figure 3.25: Pressure Distribution for Design 3

The simulation results indicate that the average outlet velocity significantly exceeds the required level, resulting in a jet-like coolant flow that impacts a smaller surface area Figure 3.24. Additionally, the inlet pressure is notably high, necessitating a

more powerful pump and potentially reducing overall system efficiency Figure 3.25. This design also consumes an excessive amount of stator core material in the main channel, adversely affecting torque production. To enhance performance, it is advisable to increase the height of the type 1 channel, which would allow the jet to cover a larger surface area and decrease the pressure drop from the main channel. Another possible improvement is to reduce the height of the main channel to conserve stator material.

3.2.5.4 Design 4

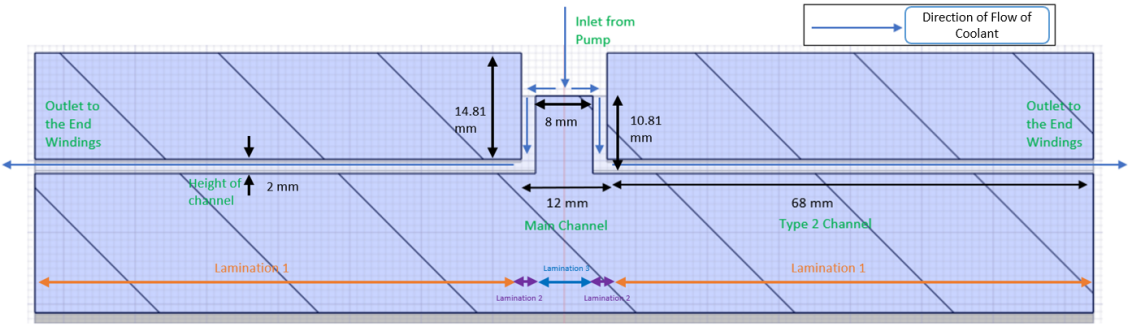

Figure 3.26: Design 4 Channel Cross-Section

Figure 3.27: Cross Section of Design 4 Outlet Face

In this iteration of the design, improvements were made to address the shortcomings of previous versions Figure 3.26. The height of the type 1 channel was increased to expand the coolant's impact area, while the main channel's height was reduced to conserve stator core material. A type 2 channel was introduced to connect the main and type 1 channels, necessitating the use of three different types of laminations for stator core manufacturing Figure 3.28. To optimize performance, the cross section of the outlet was designed as elliptical instead of rectangular, minimizing the wetted surface area and promoting a more uniform coolant flow Figure 3.27. The reduced size of the main channel further ensures an even distribution of coolant across all channels.
Material utilized - 1.96%
The results for this specific design indicate that the average velocity at the outlet closely aligns with the target value, and the pressure remains within acceptable limits. Additionally, the material loss due to the channels is minimized, with only 1.96% of the volume lost, making it the most efficient design among those simulated. Additionally, Figure 3.31 compares the average outlet velocity and inlet pressure for each design. The results indicate that Design 4 achieves the highest average outlet velocity among the designs. Although Design 4 also exhibits the highest inlet

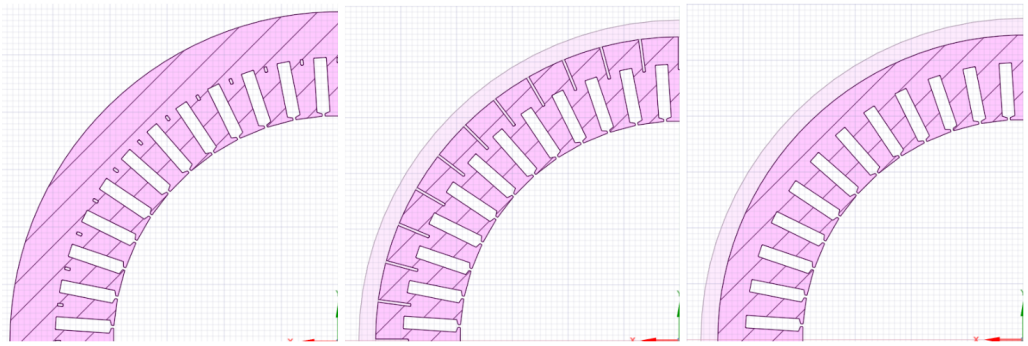

Figure 3.28: Laminations for Design4

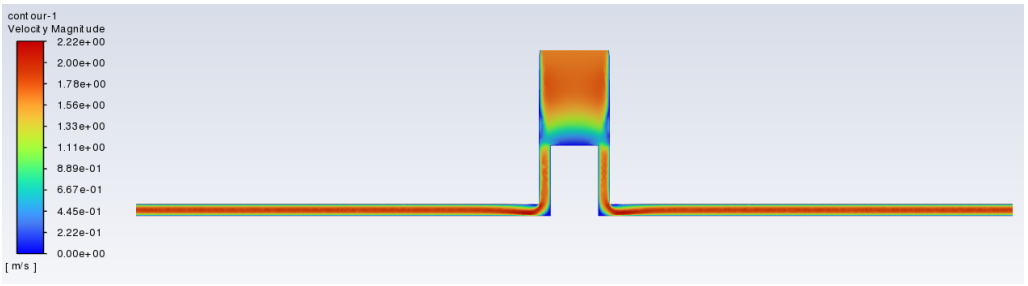

Figure 3.29: Velocity Distribution for Design 4

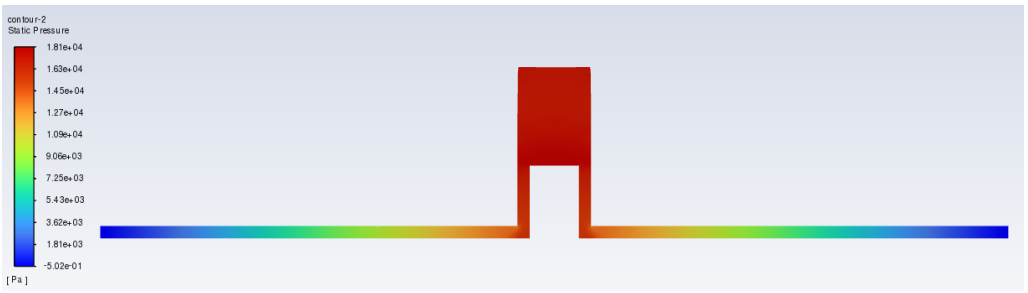

Figure 3.30: Pressure Distribution for Design 4

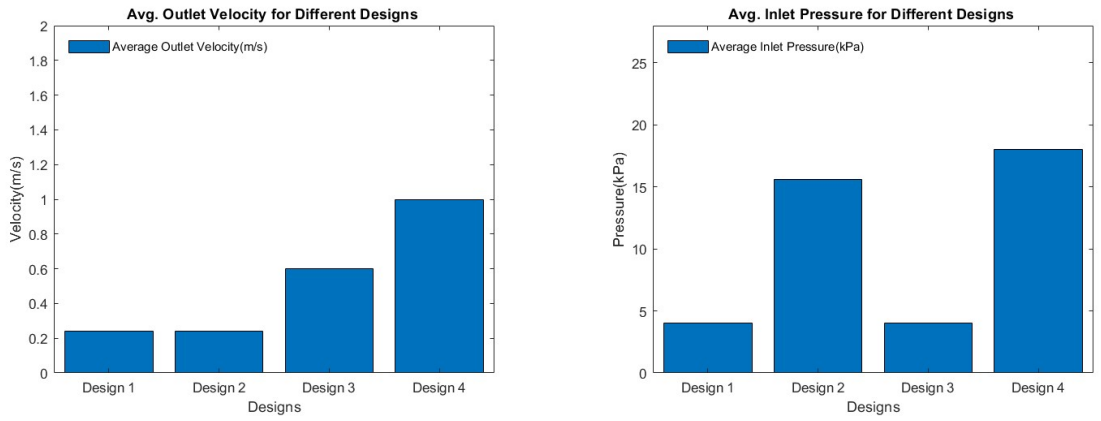

Figure 3.31: Average Outlet Velocity(Left) and Average Inlet Pressure(Right) for Different Designs

pressure, this pressure remains within the operational limits of the existing pump, making it a feasible option.

3.3 Transient Simulation

In the previous section, a steady-state simulation was conducted to determine the design that best meets the target outlet velocity and inlet pressure. In this section, a transient simulation is performed to verify whether the coolant's trajectory from the channel outlets effectively reaches the designated zones on the endwinding. Additionally, the transient simulation aims to obtain the heat transfer coefficient (HTC) values for the surfaces in contact with the coolant, providing crucial data for assessing thermal performance. The simulation was carried out in Particle Works software. Particleworks is an advanced simulation software that utilizes the Moving Particle Simulation (MPS) method, a mesh-free approach particularly advantageous for modeling transient fluid flow dynamics. Unlike traditional grid-based CFD methods, Particleworks leverages particles to simulate fluids, which simplifies the handling of complex fluid interactions such as splashing and mixing, typical in transient scenarios. The mesh-free nature of Particleworks not only enhances flexibility in simulating complex geometries but also significantly reduces preprocessing time and effort. This aspect is crucial for transient fluid flow simulations, where dynamic changes often necessitate frequent adjustments.
The particle size was selected as 0.2 mm and the time step was given as 2e-05 sec. The flow rate was set to 11 Lpm and the duration of the simulation was 0.4 sec.
The transient simulation results show that the average outlet velocity closely aligns with the outcomes from steady-state simulations. This consistency suggests that the fluid flow is expected to achieve the target velocity as predicted in the projectile calculations.
On the Drive End (DE) winding side, it has been observed that the coolant projectile does not fully reach the end of the end winding due to its upward inclination. This design configuration presents both advantages and disadvantages.
A key advantage is the generation of a splashing effect when the coolant impacts the end winding. This impact causes the coolant to deflect, thereby striking the stator core surface and the outer portions of the active windings within the stator core. After the initial impact, the coolant that adheres to the end winding surface drips downward, guided by the inclination towards the inner portion of the end winding. This mechanism enhances cooling efficiency in this region by effectively cooling both the stator core surface and the active windings on the DE side.
However, a notable disadvantage is that the coolant does not reach the most distant areas of the DE end winding in the upper section, limiting the cooling effectiveness in these regions.
On the Non-Drive End (NDE) side, as shown in Figure **??**, the coolant distribution is less uniform across the end winding quadrants compared to the Drive End (DE) side. Unlike the DE side, the coolant on the NDE side does not exhibit significant splashing (refer to Figure **??**), leading to insufficient cooling in the outer regions of the active windings and minimal contact with the stator core surface. However, the overall wetted surface coverage is still promising. Given the high thermal conduc-

tivity of copper, it is not essential to achieve complete surface coverage for effective cooling performance.

The next step in this analysis involves exporting the heat transfer coefficient (HTC) values from all surfaces in contact with the coolant. These HTC values will be employed in a subsequent thermal simulation to evaluate the cooling mechanisms within the design. This process is essential for verifying the system's capability to maintain optimal temperature levels across the stator components during operation. Additionally,Figure 3.34 shows that the average outlet velocity across the six outlets is fairly consistent, with the maximum occurring at outlet 1 and the minimum at outlet 2. Moreover, inFigure 3.2 the maximum percentage difference between the transient and steady-state CFD simulations is observed to be less than 15%, confirming that the simulations are within an acceptable range for further analysis.

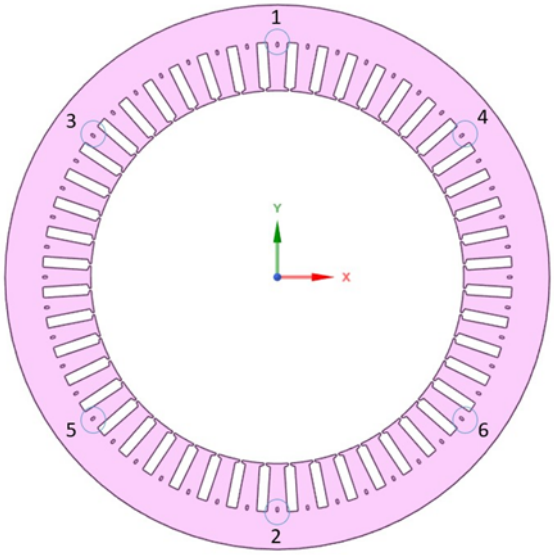

Figure 3.32: Probe Positions for Output Velocity

Channel Number	Average Velocity(m/s)	Percentage Difference from Steady State Simulation(%)
Channel No.1	1.086	2.86
Channel No.2	0.871	14.27
Channel No.3	0.935	6.87
Channel No.4	0.937	6.76
Channel No.5	0.880	13.12
Channel No.6	0.880	12.95

Table 3.2: Comparison of Transient vs. Steady-State Average Velocity

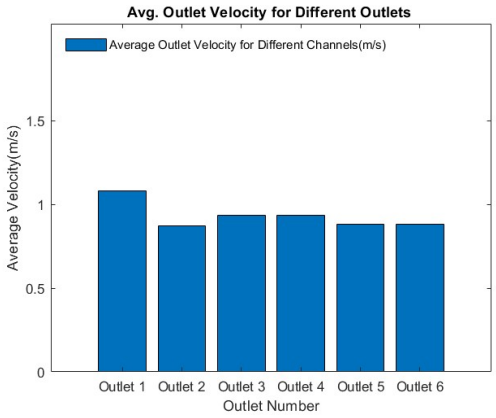

Figure 3.33: Transient Avg. Outlet Velocity for Different Outlets

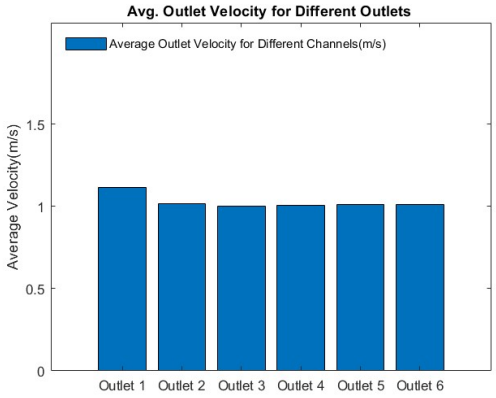

Figure 3.34: Steady State Avg. Outlet Velocity for Different Outlets

3.3.1 HTC and Thermal Contact Calculation using Lump Model

The endwinding is coated with an enamel layer, similar to the insulation around the active winding, which electrically isolates the wires from one another. The heat generated by the copper wire is conducted through this enamel layer, and on the opposite side, the coolant from the Type 1 channel outlet directly impacts this layer. To gain a deeper understanding of the cooling process, we developed a lumped system model that represents all the components involved in this heat transfer and cooling.Figure 3.35.

From Figure 3.35, It was observed that the thermal resistance of the insulation falls between the convective thermal resistance of the coolant and the thermal resistance of the copper wire. In Ansys, thermal resistance can only be specified as thermal conductance, particularly when two bodies are in contact. This specific condition is challenging to replicate because, in the CAD model, the copper wires are modeled as being in direct contact with the environment. Due to the complexity of the endwinding design, adding a solid insulation layer would further complicate the meshing and simulation process. To address this, the convection resistance was combined with the insulation resistance, resulting in a modified convection resistance. This was

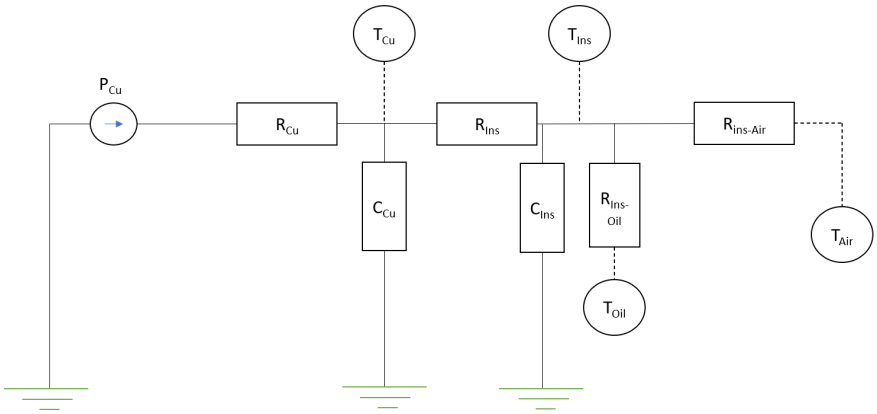

Figure 3.35: Lump Model for End Winding

then converted into a Heat Transfer Coefficient (HTC), which could be applied as a boundary condition in Ansys Thermal.
The general relation between the heat transfer coefficient (HTC) and the insulation resistance R_{ins} is given by:

$$h = \frac{l}{R \cdot A} \tag{3.10}$$

where h is the HTC, R is the resistance of the material, and A is the surface area in contact with the fluid.
The combined equation for HTC can be written as:

$$\frac{1}{h_t} = \frac{1}{h_{\text{oil}}} + \frac{t_{\text{ins}}}{K_{\text{ins}}} \tag{3.11}$$

Thus, the final HTC h_t can be expressed as:

$$h_t = \frac{K_{\text{ins}} \cdot h_{\text{oil}}}{K_{\text{ins}} + t_{\text{ins}} \cdot h_{\text{oil}}} \tag{3.12}$$

where:

- K_{ins} is the thermal conductivity of the enamel,
- h_t is the final HTC of the coolant and insulation,
- h_{oil} is the HTC for oil,
- t_{ins} is the thickness of the enamel layer.

The above equation is used in MATLAB to convert all the HTC data from the transient simulation of the coolant to the final HTC that includes the effect of insulation on the coolant HTC (Appendix C).
The electric machine is composed of various components that are assembled together, but small air pockets can still form between them, which must be accounted for in the thermal simulation. An example is the contact between the stator core and the housing. Additionally, a thin insulating material, known as a slot liner, is placed inside the stator slots to electrically insulate the wires from the metallic core, thereby preventing short circuits and electrical leakage. In this simulation, the slot liner was

modeled using thermal resistance. As previously mentioned, in Ansys, thermal resistance is represented as thermal conductance.
The thermal resistance for the slot liner R_{sl} is given by:

$$R_{\mathrm{sl}} = \frac{L_{\mathrm{sl}}}{K_{\mathrm{sl}} \cdot A_{\mathrm{sl}}} \tag{3.13}$$

where:

- R_{sl} is the thermal resistance of the slot liner,
- L_{sl} is the thickness of the slot liner,
- K_{sl} is the thermal conductivity of the slot liner,
- A_{sl} is the area of the slot liner.

The thermal conductance of the slot liner C_{sl} can be expressed as:

$$C_{\mathrm{sl}} = \frac{1}{R_{\mathrm{sl}}} \tag{3.14}$$

Similarly, the thermal conductance of the contact between housing and stator core can be calculated.

3.3.2 Thermal Simulation

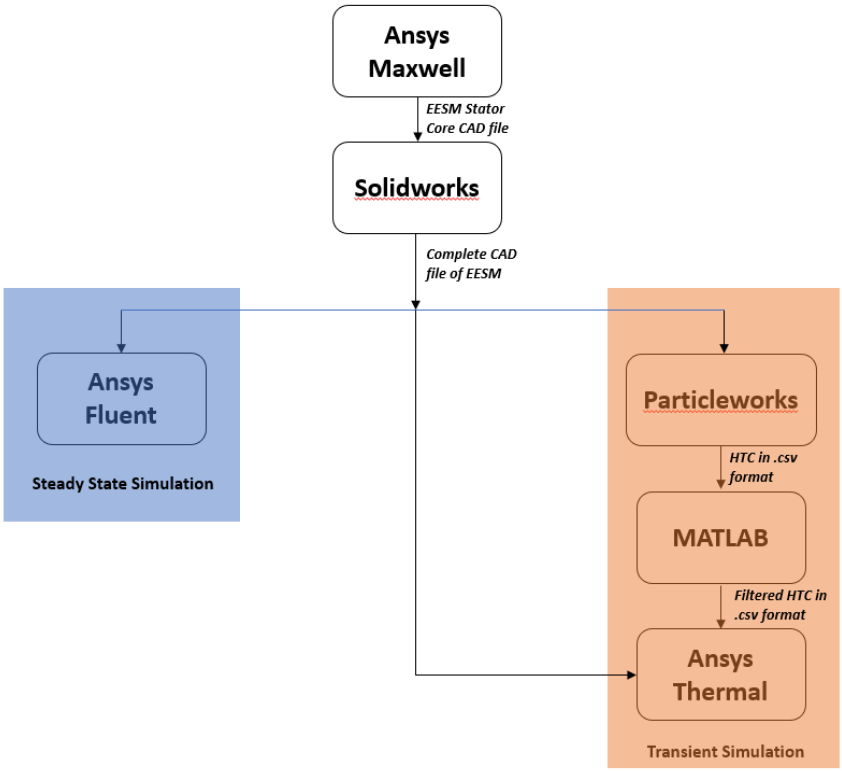

Figure 3.36: Workflow for Steady State and Transient Simulation

The simulation was conducted to analyze the temperature distribution in the EESM (Electrically Excited Synchronous Machine). The primary sources of heat generation in the EESM are copper losses and core losses. Copper losses result from the heat

produced by AC current in the stator windings and DC current in the rotor windings. In this model, 100% of the copper loss from AC current in the stator and 100% of the copper loss from DC current in the rotor were accounted for. However, in the end windings, only 20% of the copper loss from AC current was considered, along with 100% of the DC copper loss.
Iron losses in the stator core, caused by changes in the magnetic field, consist of hysteresis loss and eddy current loss. To accurately represent these heat sources, three heat generation conditions were applied as boundary conditions in the simulation.
The materials used in the simulation were characterized by their thermal conductivity, with the specific values corresponding to the temperatures of the coolant flow Figure 3.3.

Material	Thermal Conductance (W/mK)	Reference Temperature (°C)
Enamel	0.5	60
Housing	168	60
Copper	387.6	60
Steel Laminate	X - 22.5 Y - 22.5 Z - 5	60

Table 3.3: Material properties for EESM

The EESM is cooled through dedicated cooling channels within the stator core, making it necessary to apply a convection boundary condition with specified heat transfer coefficients (HTCs) in W/m²K. To obtain the HTC data, a transient CFD simulation was initially conducted with a 11 L/min flow rate at 60°C. The coolant entered the channels from the bottom of the machine. The resulting HTC data was exported in .csv format and processed in MATLAB for filtration Figure 3.36. During this process, any data disturbances were removed, the data was adjusted to align with the origin position in the Ansys model, and a temperature column was added. The processed data was then mapped onto the model in Ansys as a convection boundary condition.
Additionally, a separate convection boundary condition was applied to surfaces in contact with the surrounding air, assigning these surfaces an HTC of 10 W/m²K. The stator's inner surface, in contact with the air gap, experiences forced convection due to the rotor's rotation. Figure 3.37 shows the change of HTC with increase of rotor speed.
Additionally, thermal resistances were incorporated at the interfaces between components. In Ansys, these thermal resistances were represented as thermal conductances.
Finally, the thermal simulation was run for 4 operating points Figure 3.4.
The machine features two endwindings: the Non-Driving End (NDE) winding and the Driving End (DE) winding. To better understand the heating distribution across both endwindings, probes were positioned at 22.5-degree intervals.

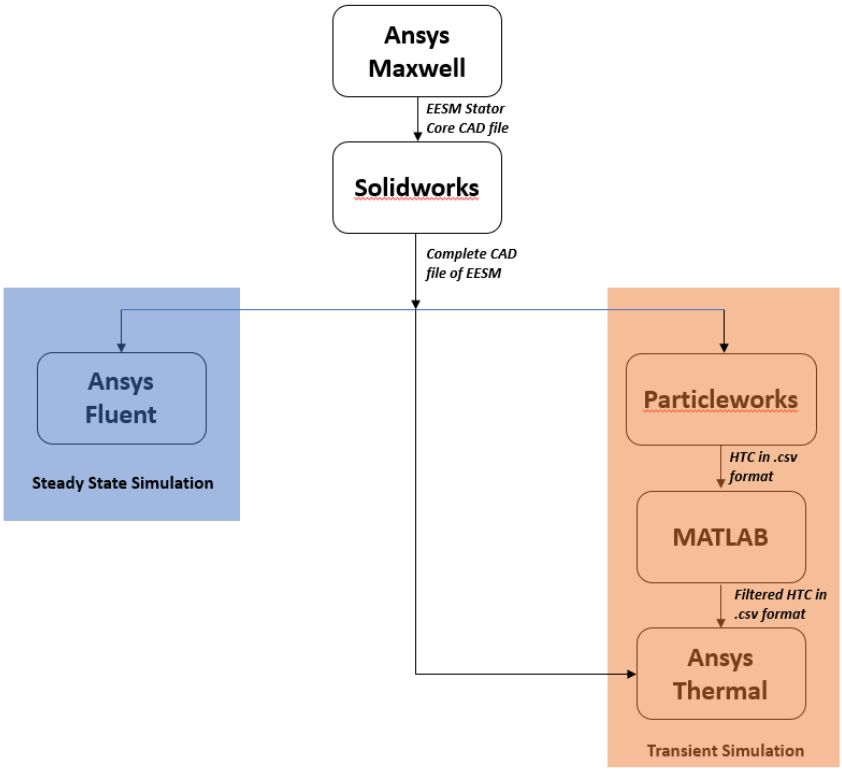

Figure 3.37: Change in HTC of stator inner surface with rotor speed

Operating Points	Speed (RPM)	Torque (Nm)	Torque Percentage(%)	Power (kW)	Power Percentage(%)	Copper Loss(W)	Iron Loss (W)	Copper Loss(W/m^3)	Iron Loss(W/m^3)
OP1	8000	223.60	46.7	187.3	47.8	2891.64	893.53	5.42e+06	3.47e+05
OP2	10000	187.01	39	195.8	49.9	2774.8	888.20	5.2e+06	3.4e+05
OP3	15000	126.01	26.3	197.9	50.5	4125.95	970.64	7.7e+06	3.77e+05
OP4	18000	104.05	21.7	196.1	50	5195.10	1086.01	9.7e+06	4.2e+05

Table 3.4: Table showing various operating points and corresponding losses

4
Results

This section presents the results from the thermal simulation described earlier. To observe the temperature distribution across the components, measurement scopes were placed at several key points, as illustrated in Figure 4.1.

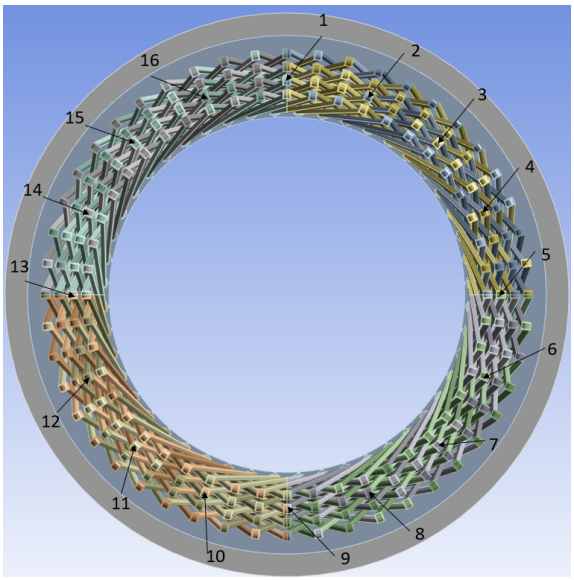

Figure 4.1: Scope Locations

4.1 Endwindings

Figure 4.2 and Figure 4.3 illustrate the temperature variations in the NDE and DE end windings. It is evident that different regions of the end windings receive varying levels of cooling, primarily influenced by how the coolant interacts with these areas. The transient CFD simulation reveals that the coolant is most effective in the North-East and South-East quadrants, resulting in better cooling in these regions. Conversely, the South-West quadrant experiences inadequate coolant coverage, leading to higher temperature zones.
This lateral non-uniform cooling can be attributed to the orientation of the upper layer of the end winding. On the right side of the NDE end winding, the upper layer is oriented upwards (refer to the first and second quadrant inFigure 4.2). On the left side, however, the upper layer points downwards (see the third and fourth quadrant in Figure 4.2). When the coolant impacts the upper layer on the right

side, it initially strikes the middle section of the winding. Some droplets reflect back, either hitting the stator core or the active winding, while the majority of the coolant drips down, covering a substantial surface of the second quadrant winding or flowing toward the stator core due to surface tension between the coolant and the end winding. This behavior enhances the heat transfer coefficient (HTC) and results in more uniform cooling.
In contrast, on the left side of the NDE end winding, where the upper layer points downwards, the coolant impacts the middle part but, due to gravity, the high-speed projectile hits the surface of the uppermost layer and subsequently reflects away from the end winding in the axial direction. This results in less effective and non-uniform cooling on the left side of the NDE end winding.
At lower flow rates, however, the velocity of the coolant is insufficient to reflect away from the end winding. Instead, it remains attached to the surface and drips down, cooling the end windings in the third quadrant more effectively.
The temperature distribution for the DE end winding is depicted in Figure 4.3. Notably, the temperature near the inner part of the end winding (adjacent to the stator core) is lower than that of the outer part in the upper section. This difference arises because the coolant stream primarily reaches the inner portion of the end winding due to its upward slope. The fluid first impacts the middle section of the DE end winding and subsequently flows downward toward the stator core. In the lower section, gravity causes the coolant stream to bend slightly, resulting in more effective cooling of the outer part compared to the inner part along the axial direction.
In the DE end winding, zones of higher temperature form predominantly on the left side, specifically in the third and fourth quadrants. The cause of these zones is similar to those observed in the NDE end winding. However, due to the upward bend of the DE end winding, the coolant cannot adequately reach the outer axial region in the upper part of the end winding, particularly in the fourth quadrant. As a result, the coolant is unable to effectively cool the outer axial portion of the end winding in the third quadrant, leading to the formation of hot zones.. As illustrated in Figure 4.3, an increase in the motor's power output corresponds with a rise in the average temperature of both end windings.

4.2 Stator Core

Heating in the stator core is primarily driven by two factors: copper losses in the active winding and iron losses within the stator core. Copper losses occur due to the resistance in the winding as current flows through it, while iron losses are caused by hysteresis and eddy currents in the core material during magnetization cycles. Together, these losses contribute to the overall temperature rise in the stator core.. Figure 4.6shows that the maximum temperature recorded is 162.47°C near the active winding on the Non-Driving End (NDE) side, while the minimum temperature is 105.93°C at operating point OP3 on the Driving End (DE) side. These results indicate that the temperatures in the stator core are consistently lower on the DE side compared to the NDE side. This temperature disparity is primarily attributed to the upward slope of the DE end winding, which allows the coolant to directly

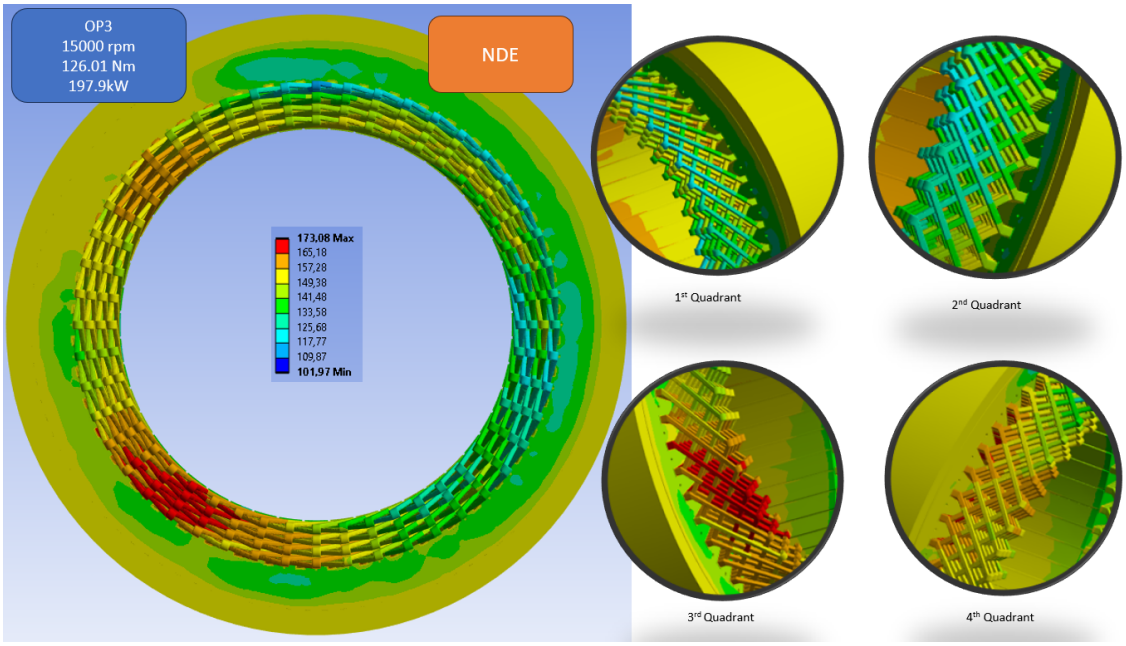

Figure 4.2: NDE End Winding Temperature Distribution at OP3

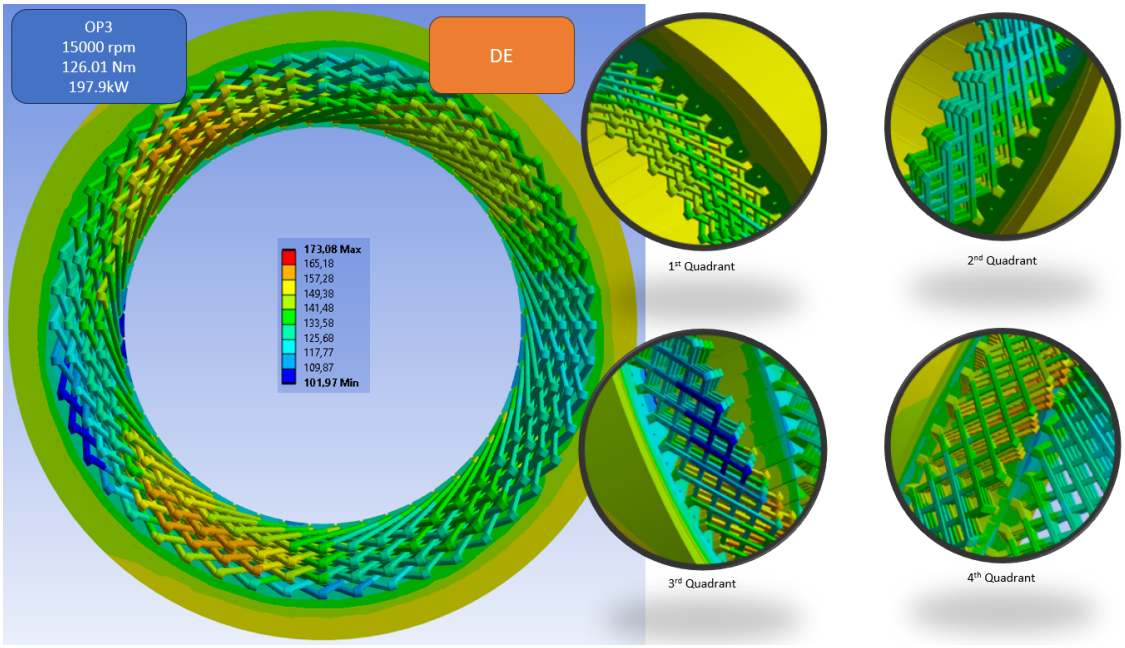

Figure 4.3: DE End Winding Temperature Distribution at OP3

impact the surface of the end winding and subsequently flow onto the stator core. This configuration enhances the heat transfer coefficient (HTC) on the DE side, leading to more efficient cooling. Figure 4.6clearly demonstrates that the lower part of the stator is cooled more effectively than the upper part. This disparity arises because, in the upper section, the coolant only partially contacts the end winding, leaving portions of its surface uncovered. In contrast, although the coolant flow in the lower part is slightly deflected by gravity, causing it to bend away from the end

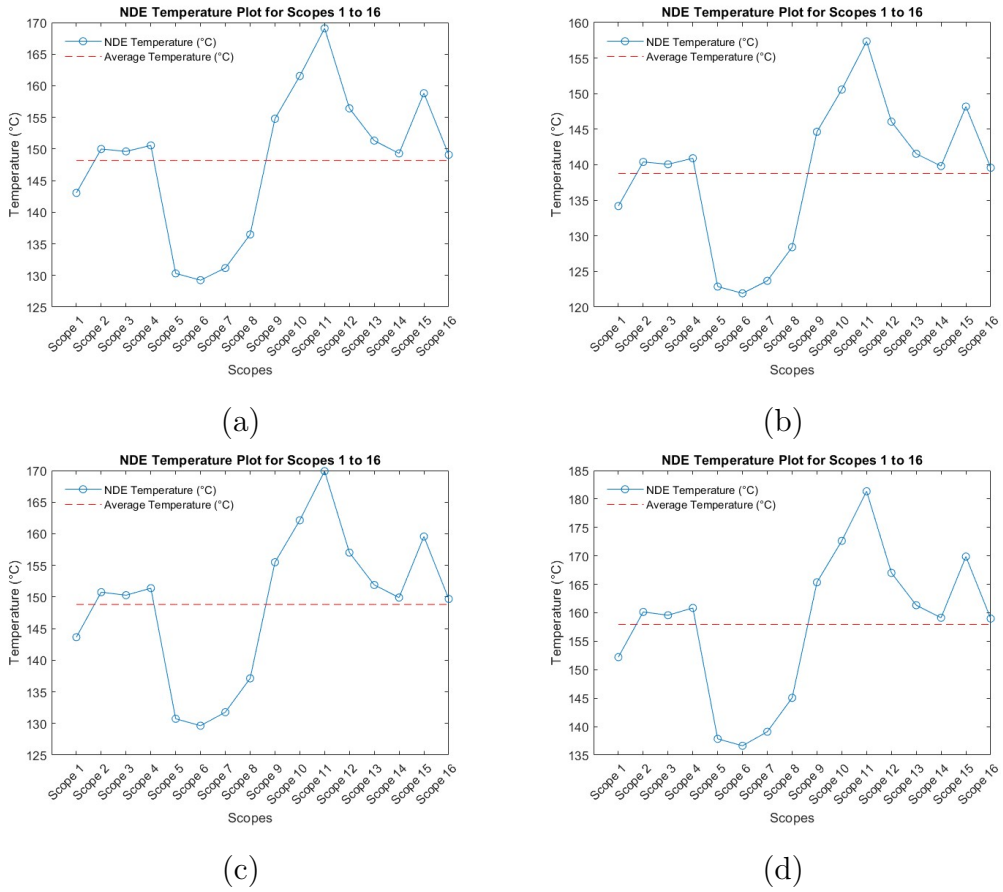

Figure 4.4: NDE Endwinding Temperature Distribution at (a) Operating Point 1, (b) Operating Point 2, (c) Operating Point 3, and (d) Operating Point 4

winding, the overflow from the upper section fully covers the lower end winding. This results in significantly better cooling performance in the lower region.

4.3 Active Windings

The active winding, primarily composed of copper, generates heat due to the current flowing through it. However, the cooling design presented in this thesis does not directly address the active winding. Implementing cooling channels from the outer surface of the stator to the inner regions would lead to substantial material loss in the stator and a consequent reduction in torque generation. Additionally, such a design would introduce significant manufacturing complexities.Figure 4.8 and Figure 4.9 illustrate the temperature distributions across the active winding in Sections 1 and 2 at various operating points. A comparison of the two reveals that temperatures in Section 1 (Figure 4.8) are consistently higher than those in Section 2 (Figure 4.8) due to superior cooling at the drive-end (DE) of the machine compared to the non-drive-end (NDE). In most graphs, the lowest temperatures occur at Scope 5 and Scope 6, which correspond to areas with better cooling, as depicted in Figure 4.4 and Figure 4.5. In Section 1, the highest temperature is recorded at Scope 11 or

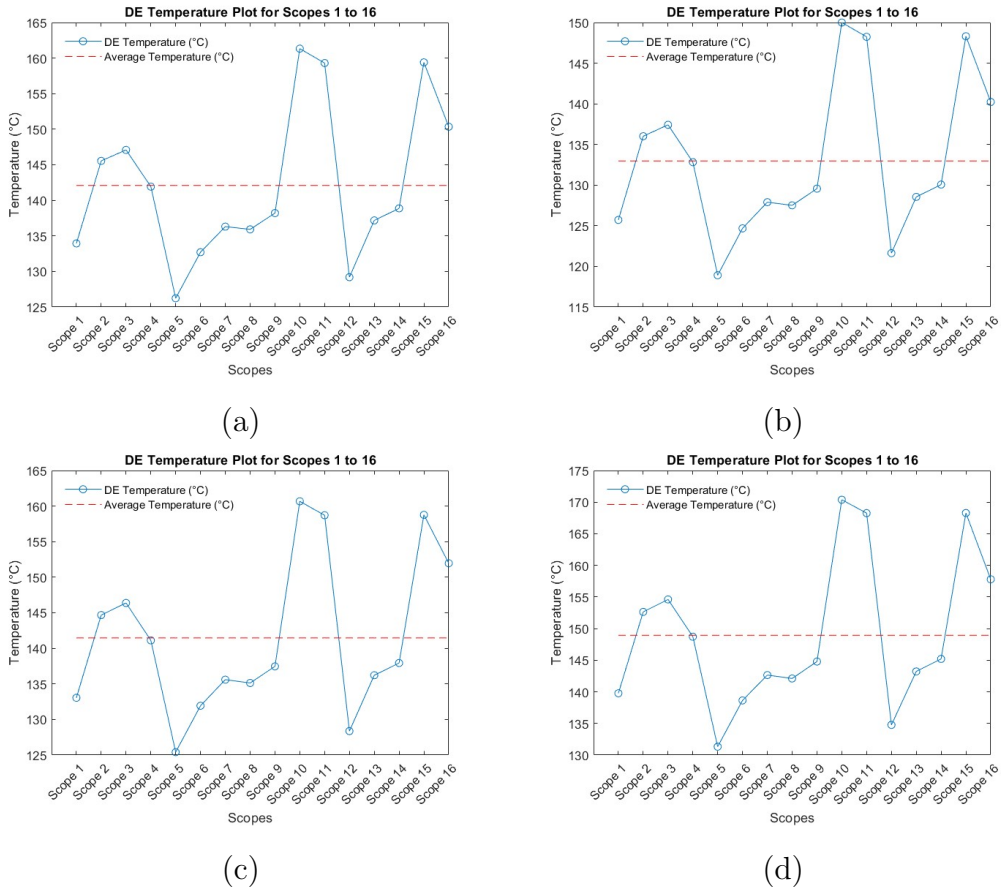

Figure 4.5: DE Endwinding Temperature Distribution at (a) Operating Point 1, (b) Operating Point 2, (c) Operating Point 3, and (d) Operating Point 4

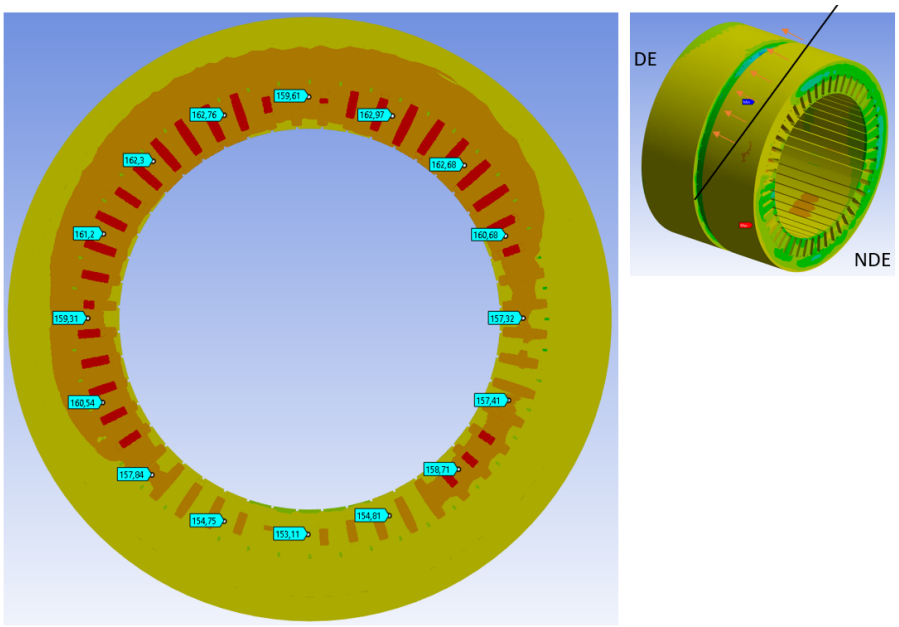

Figure 4.6: NDE Side Stator Sectional View (Section 1)

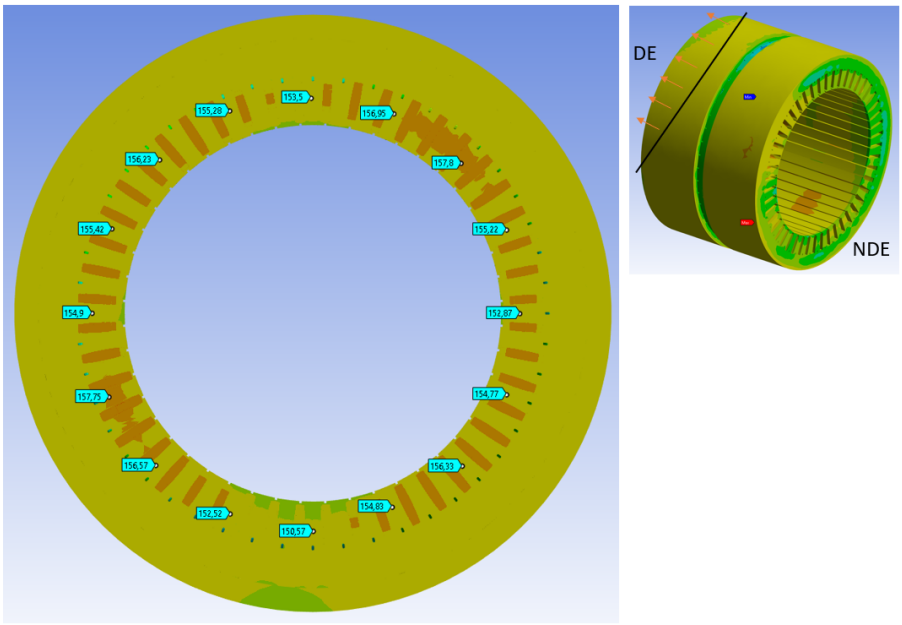

Figure 4.7: DE Side Stator Sectional View (Section 2)

Scope 12, aligning with the NDE end winding, where Scope 11 shows the maximum temperature. In contrast, Section 2 registers a lower temperature at Scope 13, which corresponds to the more effective cooling of the DE end winding in this region, as shown in Figure 4.5. Overall, the active winding reaches a peak temperature of approximately 186°C at operating point OP4 at Scope 11. Additionally, the temperature variance in Section 2 is lower than in Section 1, indicating that while the cooling system effectively reduces heat in specific areas, particularly near the DE side, there is room for improvement. Enhancing the cooling system to better address thermally stressed regions on the NDE side would result in a more uniform temperature distribution and improved operational efficiency.

4.4 Enamel

The enamel serves as the insulation layer on the copper wires, providing electrical isolation both between the wires and from the surrounding environment to prevent electrical faults. It is designed to withstand high temperatures, ensuring that the windings do not degrade or short-circuit due to thermal stress. Being in direct contact with the copper wire, the enamel operates at elevated temperatures, as illustrated in the figure below.

4.5 Housing

The housing provides crucial structural support for the machine, securing all components in place and maintaining proper alignment during operation. It also plays a role in thermal management by directing coolant flow and dissipating heat through its external surfaces. While the housing is less impacted by the heat generated from

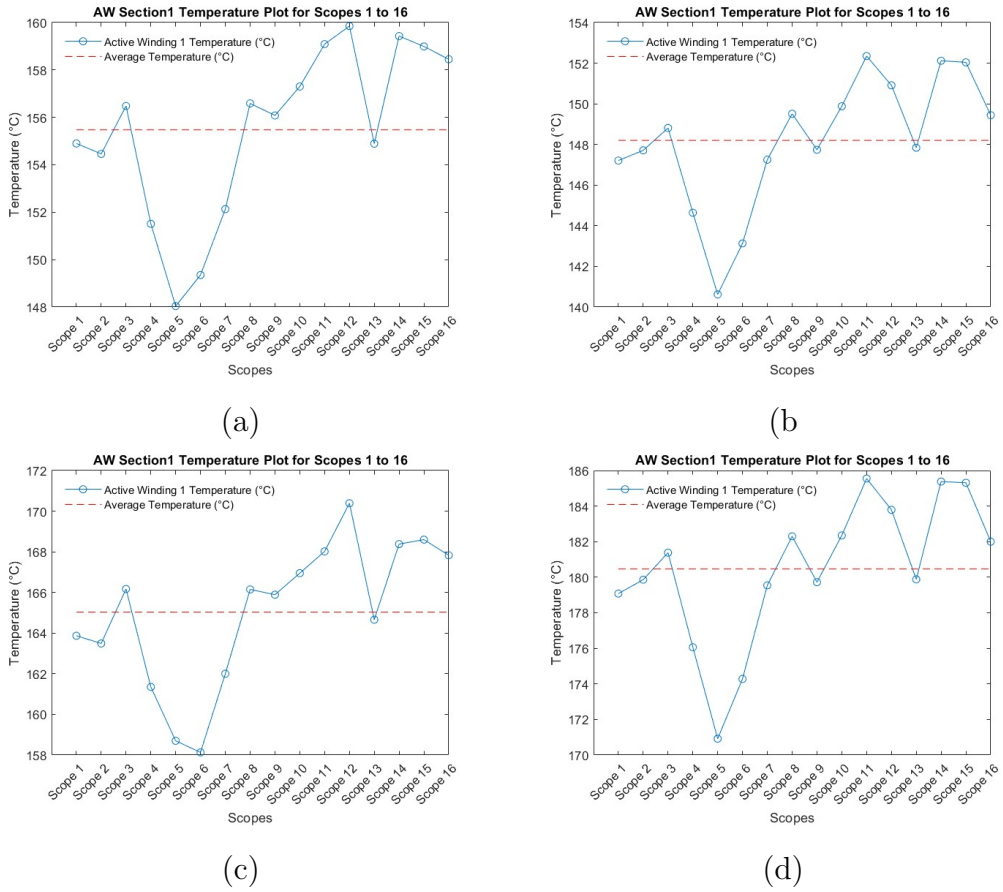

Figure 4.8: Active Winding Section 1 Temperature Distribution at (a) Operating Point 1, (b) Operating Point 2, (c) Operating Point 3, and (d) Operating Point 4

copper losses, it does experience heating primarily due to iron losses. Compared to other components, the housing generally heats up to a lesser extent.

4.6 Comparison of Maximum and Average Temperatures Across Different Components

Based Figure **??**, all components show a temperature dip at the second operational point, followed by a rise in temperature at the third and fourth operational points. Among the components, the active winding reaches the highest temperatures, followed by the enamel, stator core, and then the housing. Comparing the maximum temperature and average temperature curves for different components provides insights into their cooling performance.

The slope of the average temperature curves for various components at different operating points indicates how effectively the cooling system controls temperature increases. The DE endwinding exhibits the lowest slope, suggesting efficient cooling. In contrast, the active winding and enamel show higher slopes, indicating more significant temperature increases with rising motor power.

The difference between the maximum temperature curve and the average temper-

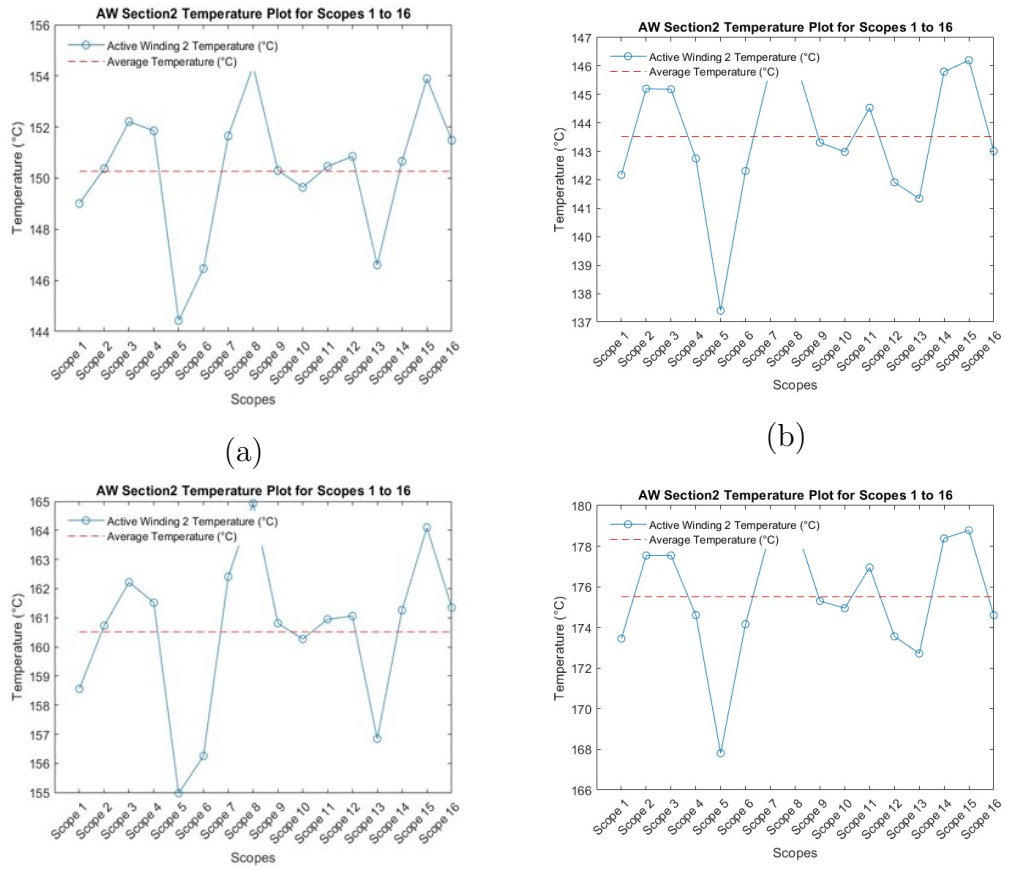

Figure 4.9: Active Winding Section 2 Temperature Distribution at (a) Operating Point 1, (b) Operating Point 2, (c) Operating Point 3, and (d) Operating Point 4

ature curve highlights the uniformity of temperature distribution within each component. The housing and active winding display the most uniform temperature distribution. The housing benefits from less heat from the stator and has a large surface area for convective heat transfer. The active winding, although not directly cooled by the coolant, shows relatively stable temperatures due to its indirect cooling.
In contrast, the endwindings exhibit a notable difference between the maximum and average temperature curves. This variation is attributed to the direct impact of coolant on the endwinding surfaces, resulting in less uniform temperature distribution.

4.7 Drive Cycle Simulations

In this section, a drive cycle simulation was conducted to evaluate the effectiveness of the designed EESM machine in propelling a real vehicle. Key data from the EESM, such as maximum torque, rotational speed, and efficiency, were exported for this purpose.

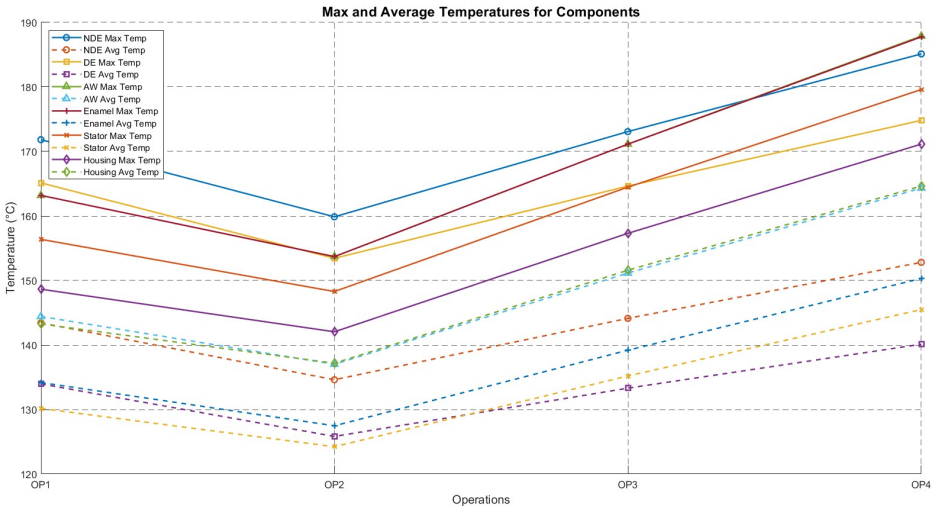

Figure 4.10: Velocity Profile for DE Transient Simulation

Model-Based Design (MBD) utilizes mathematical models to simulate real-world conditions by representing systems through equations. This methodology enables testing and validation of designs prior to the construction of physical prototypes. By integrating design, simulation, and automatic code generation, MBD significantly reduces both development time and costs. In this case, MBD was applied using equations and detailed information about the vehicle architecture, along with specific drivetrain parameters such as wheel size, gear ratios, and battery specifications.

4.7.1 Vehicle model

The vehicle model was developed based on the force equations acting on a moving vehicle. The primary force responsible for the vehicle's acceleration is the traction force, which is generated by the propulsion system and transferred to the wheels via the gear system. For the vehicle to move forward, the traction force must exceed the resistive forces acting on the vehicle.

In addition to the traction force, several resistive forces reduce its effectiveness. One of these is aerodynamic force, which arises from air resistance as the vehicle moves through the atmosphere. Aerodynamic forces include drag, which opposes the vehicle's motion, and lift, which can either push the vehicle upwards or downwards, depending on its design. As speed increases, drag becomes more significant, impacting the vehicle's range, making aerodynamics a critical factor in vehicle design.

Gradient force occurs when the vehicle is driven on an incline or slope. This force opposes motion when driving uphill, requiring more power from the propulsion system, and assists when moving downhill. The magnitude of this force depends on the steepness of the slope and the weight of the vehicle, influencing both range and performance on varying terrains.

Frictional force arises from the interaction between the tires and the road surface, facilitating vehicle control, acceleration, and braking. While it provides the necessary grip for traction, it also opposes motion. The amount of friction depends

on factors such as tire material, road conditions, and the vehicle's weight, directly impacting vehicle stability, handling, and overall range.
This version maintains the necessary clarity and formal tone required for a thesis.
The traction force is represented as,

$$F_t = m \cdot a \tag{4.1}$$

F_t is the force by pure acceleration on the vehicle, m is mass of the vehicle and a is vehicle acceleration.
The aerodynamic force is represented as,

$$F_d = \frac{1}{2} \cdot C_d \cdot \rho \cdot A_r \cdot u^2 \tag{4.2}$$

F_d is the aerodynamic drag force on the vehicle, C_d is drag coefficient, ρ is air density, A_r is reference area and u is velocity of the vehicle.
The gradient force is represented as,

$$F_g = m \cdot g \cdot \sin(\theta) \tag{4.3}$$

Here F_g is the gradient force on the vehicle,θ represents the road inclination and g represents the force due to gravity.
The frictional force is represented as,

$$F_f = \mu \cdot F_n \tag{4.4}$$

F_f is the frictional force on the vehicle, μ is the coefficient of friction between tyre and road. F_n is the normal force.
The net force required to propel the vehicle can be represented as,

$$F_{\text{net}} = F_t - F_g - F_f - F_d \tag{4.5}$$

F_{net} is the net force on the vehicle.
This model takes vehicle velocity, acceleration, and road inclination as inputs. After accounting for various resistances, such as aerodynamic drag and rolling resistance, it outputs the vehicle's velocity, acceleration, and the required force to propel the vehicle.

4.7.2 Wheel model

In this model, the force required to propel the vehicle is translated into torque on each drive wheel. Additionally, the model converts the vehicle's linear velocity into the angular velocity of the wheels, and similarly, the linear acceleration of the vehicle is converted into angular acceleration.

$$F_{\text{wheel}} = \frac{T_{\text{wheel}}}{r_{\text{wheel}}} \tag{4.6}$$

F_{wheel} is the force at the wheel (in Newtons, N). T_{wheel} is the torque applied at the wheel (in Newton-meters, Nm). r_{wheel} is the radius of the wheel (in meters, m).

$$v_{\text{wheel}} = r_{\text{wheel}} \cdot w_{\text{wheel}} \tag{4.7}$$

v_{wheel} is the linear velocity of the wheel (in meters per second, m/s). r_{wheel} is the radius of the wheel. w_{wheel} is the angular velocity of the wheel (in radians per second, rad/s).

$$a_{\text{wheel}} = r_{\text{wheel}} \cdot \alpha \tag{4.8}$$

a_{wheel} is the linear acceleration of the wheel (in meters per second squared, m/s^2). r_{wheel} is the radius of the wheel. α is the angular acceleration of the wheel (in radians per second squared, rad/s^2).

4.7.3 Gear Ratios

This model represents the gear system connecting the wheels to the motor. The gear ratio defines the relationship between the number of teeth on two meshing gears. A higher gear ratio from the wheels to the motor results in higher motor speed and lower torque relative to the wheels. Selecting an appropriate gear ratio is crucial for optimizing vehicle performance, as it balances acceleration, top speed, and motor efficiency, particularly in electric and hybrid vehicles.

$$GR = \frac{N_{\text{motor}}}{N_{\text{wheel}}} = \frac{T_{\text{wheel}}}{T_{\text{motor}}} = \frac{\omega_{\text{motor}}}{\omega_{\text{wheel}}} \tag{4.9}$$

N_{motor} and N_{wheel} are the rotational speeds (RPM) of the motor and the wheel, respectively. T_{motor} and T_{wheel} are the torques at the motor and the wheel, respectively.ω_{motor} and ω_{wheel} are the angular velocities of the motor and the wheel, respectively.

4.7.4 Electric Machine

The electric machine model used in this study incorporates a lookup table, with the speed of the EESM as the row values, the torque as the column values, and the table values representing the efficiency of the EESM. This efficiency data was obtained through simulations conducted in Ansys Maxwell. The torque and speed demands from the gearbox model are then plotted on the EESM's efficiency map, which was generated using the lookup table. For each operating point, the torque, speed, and efficiency of the motor are used to calculate the power required from the motor, including the auxiliary power. This required power is subsequently communicated to the battery model, which supplies the necessary power based on its available capacity.

4.7.5 Battery model

The battery model employed in this study calculates the required current by dividing the power demand from the machine by the current battery voltage. This current is then distributed among the individual cells by dividing it by the number of parallel branches in the battery pack. The current for each cell is subsequently converted to capacity, and depending on whether the battery is charging or discharging, the

capacity change due to the power demand is either added to or subtracted from the initial capacity. This process provides the current state of charge (SOC) of the battery.
Using the current SOC, the open-circuit voltage (OCV) for each cell is determined based on the manufacturer-provided OCV vs. SOC curve. Additionally, internal resistance data as a function of SOC, obtained from the manufacturer, is used through a lookup table to calculate the terminal voltage of each cell, as well as for the entire battery pack. This resistance data also allows for the calculation of power losses within the battery.
Battery current can be calculated as,

$$I_{\text{battery}} = \frac{P_{\text{battery}}}{V_{\text{terminal}}} \tag{4.10}$$

$$V_{\text{terminal}} = V_{\text{oc}} - I \cdot R_{\text{int}} \tag{4.11}$$

V_{terminal} is the terminal voltage of the battery pack, V_{oc} is the open-circuit voltage, I is the current flowing through the battery, R_{int} is the internal resistance of the battery.
I_{battery} is the total current flowing through the battery pack and P_{battery} is the power output (or input) of the battery pack.

$$I_{\text{cell}} = \frac{I_{\text{battery}}}{N_{\text{parallel}}} \tag{4.12}$$

I_{cell} is the current flowing through each individual cell and N_{parallel} is the number of cells connected in parallel in the battery pack.

$$Q_{\text{used}}(t) = \int I_{\text{cell}}(\tau)\, d\tau \tag{4.13}$$

$Q_{\text{used}}(t)$ is the total charge used over time t, typically in Ampere-hours (Ah), $I_{\text{cell}}(\tau)$ is the current flowing through the cell at time τ.

$$\text{SOC}(t) = \left(\frac{Q_{\text{remaining}}(t)}{Q_{\text{initial}}} \right) \times 100 \tag{4.14}$$

$\text{SOC}(t)$ is the state of charge at time t, expressed as a percentage, $Q_{\text{remaining}}$ is the remaining charge in the cell at time t and Q_{initial} is the initial charge of the cell, typically the rated capacity of the battery.

$$\text{SOC}(t) = \text{SOC}_0 - \left(\frac{1}{Q_{\text{battery}}} \int I(\tau)\, d\tau \right) \tag{4.15}$$

$\text{SOC}(t)$ is the state of charge at time t, SOC_0 is the initial state of charge, Q_{battery} is the battery capacity (in Ah), $I(\tau)$ is the current at time τ.

4.7.6 Results for Drive cycle Simulation

The Drive cycle simulations were run for 3 vehicles to check how the EESM machine was performing. The drive cycle used for the simulation was WLTC. The WLTC (Worldwide Harmonized Light Vehicles Test Cycle) is a global standard used to assess vehicle fuel efficiency and emissions. It simulates real-world driving with urban, suburban, and highway phases, providing more accurate data than older cycles like NEDC. The test adapts to different vehicle types based on their power-to-weight ratio (Appendix D).
Following Figure 4.1 is the vehicle data used,

Vehicle Model	Nissan Leaf FWD	Tesla Model 3 RWD	Mercedes EQS580 AWD	BMW iX xDrive50 AWD
Total Mass(kg)	1596	1725	2585	2585
Vehicle Cross-Section Front(m2)	2.27	2.22	2.51	2.82
Drag Coefficient	0.29	0.23	0.2	0.25
Rolling Coefficient	0.009	0.009	0.009	0.009
Wheel Diameter(m)	0.6129	0.6505	0.7153	0.7663
Gear Ratio	8.193	9	Front 9.72 Rear 9.64	Front 8.77 Rear 11.22
Efficiency	0.97	0.97	0.97	0.97
No. of Cells in Series	96	106	108	100
No. of Cells in Parallel	2	1	4	2
Cell Capacity (Ah)	57.1	176.5	75.8	85.6

Table 4.1: Sample table with 4 columns and 15 rows

Analysis of Figure 4.11, reveals that the operating points for all four vehicles under the WLTC drive cycle fall within the torque-speed limits of the EESM machine. In the current configurations of the Nissan Leaf and Tesla Model 3 RWD, the EESM exhibits a higher power capacity than required, causing their operating points to cluster in the low-speed, low-torque region, which is a less efficient operating zone for the machine. To enhance efficiency in these vehicles, increasing the gear ratio (between the wheels and the machine) could shift the operating points into a more efficient region of the EESM's performance map.
The Mercedes EQS580 and BMW iX xDrive50 AWD employ separate motors and transmissions for the front and rear axles, effectively distributing the load across the vehicle. This driveline architecture is the reason the operating points for each motor in the Mercedes EQS580 resemble the single motor operating points observed in the Nissan Leaf FWD and Tesla Model 3 RWD. Notably, the operating points for both motors in the Mercedes EQS580 appear very similar, which can be attributed to the nearly identical gear ratios used for the front and rear axles. The maximum torque required by each motor is slightly below 150 Nm, approximately 30% of the EESM's maximum torque, suggesting that two lower-powered EESM machines could be well-suited for this powertrain. In contrast, the BMW iX xDrive50 AWD exhibits significant differences in gear ratios between its front and rear motors, as illustrated in Figure 4.11(a) and Figure 4.11 (b). This vehicle also has the largest wheels among the compared vehicles, requiring the motor to deliver more torque. Additionally, its larger frontal cross-section leads to higher aerodynamic drag. The rear motor operates across a broader speed range than the front motor. The maximum torque observed at any operating point reaches 70% of the EESM's maximum torque, indicating that the machine can accommodate even higher torque demands.

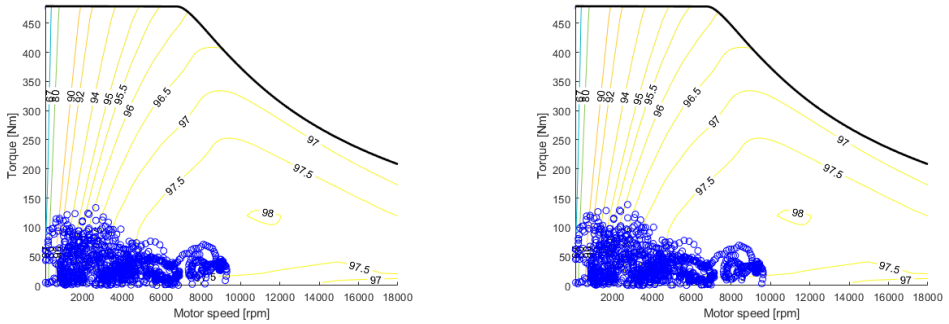

(a) Nissan Leaf FWD (b) Tesla Model 3 RWD

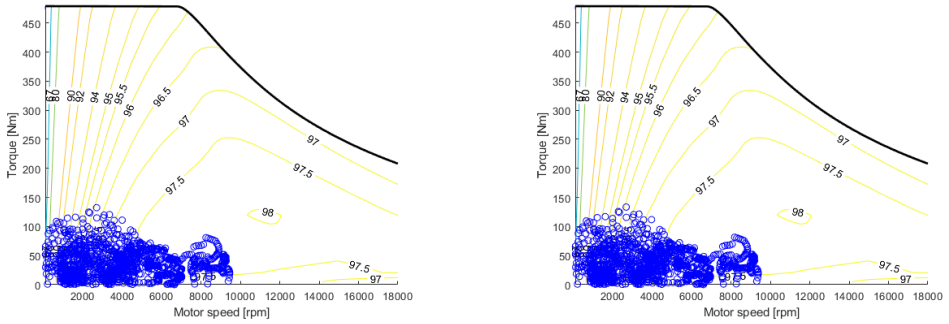

(c) Mercedes EQS580 AWD (Front) (d) Mercedes EQS580 AWD (Rear)

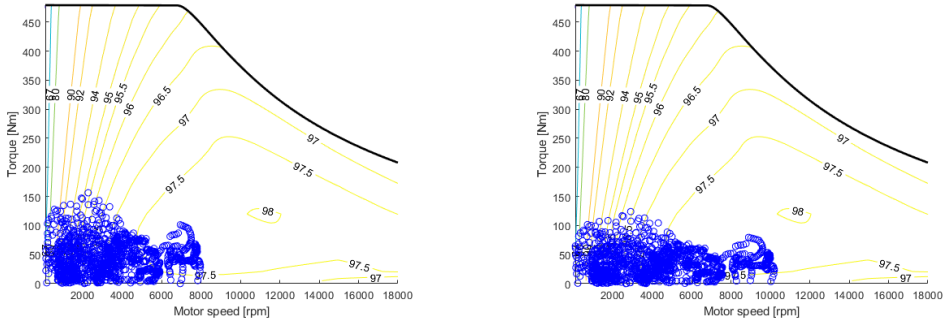

(c) BMW iX xDrive50 AWD (Front) (d) BMW iX xDrive50 AWD (Rear)

Figure 4.11: Operating points for different vehicles using EESM

These vehicles were not originally designed to be an optimal match for the EESM; therefore, adjusting certain vehicle parameters, such as the gear ratio, can significantly enhance vehicle performance. In Figure 4.12, the Gear Ratios (GR) for the vehicles were increased by two and six to evaluate the impact on vehicle performance. Figure 4.12 (a) and Figure 4.12 (b) increasing the gear ratio (from wheels to machine) causes the operating points of the vehicle to shift into more efficient regions of the machine. This adjustment improves the vehicle's range and reduces overall energy losses.
It is important to note, however, that the vehicle models used in this analysis may not fully reflect the actual performance characteristics, as manufacturers do not provide complete information on their drivetrains.

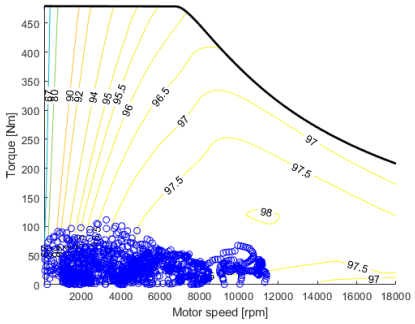

(a) Mercedes EQS580 AWD GB+2 (Front)

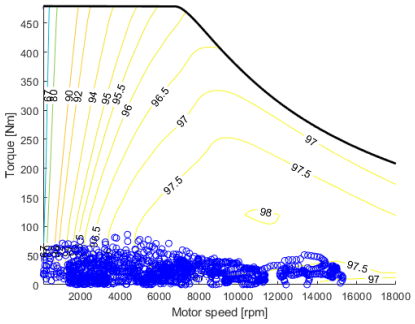

(b) Mercedes EQS580 AWD GB+6 (Front)

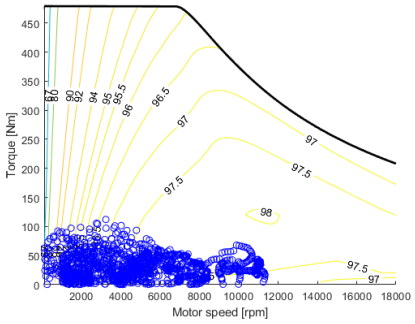

(c) Mercedes EQS580 AWD GB+2 (Rear)

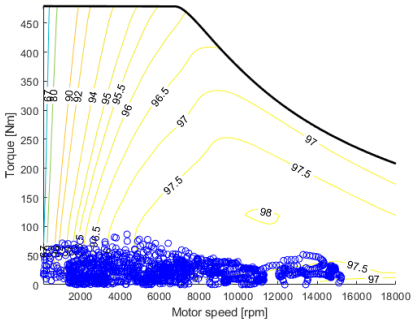

(d) Mercedes EQS580 AWD GB+6 (Rear)

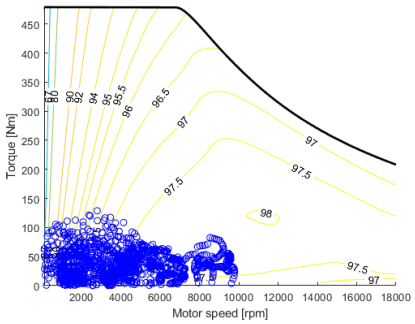

(e) BMW iX xDrive50 AWD GB+2 (Front)

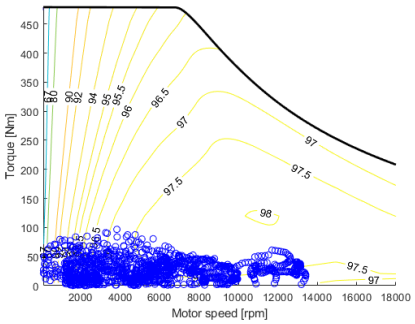

(f) BMW iX xDrive50 AWD GB+6 (Front)

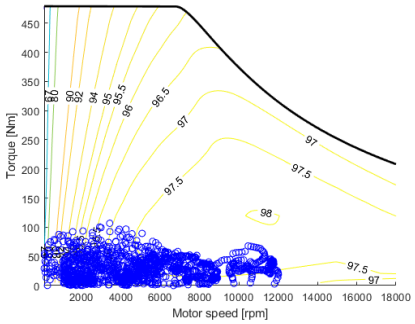

(g) BMW iX xDrive50 AWD GB+2 (Rear)

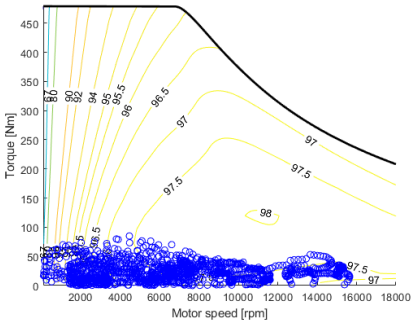

(h) BMW iX xDrive50 AWD GB+6 (Rear)

Figure 4.12: Operating points for different vehicles using EESM

5
Conclusion

This thesis has successfully addressed the thermal management challenges in Electrically Excited Synchronous Machines (EESMs) by integrating loss analysis, cooling channel design, and advanced simulation techniques. Initially, the study focused on identifying and quantifying the various losses occurring within the machine, including copper and iron losses, using Ansys Maxwell. These findings provided the foundation for designing cooling channels aimed at mitigating the thermal stresses associated with high-speed operation.
Four distinct cooling channel designs were developed based on projectile calculations and subsequently evaluated through steady-state CFD simulations in Ansys Fluent. The most effective design was selected based on its ability to achieve the desired cooling performance while maintaining structural and operational feasibility.
To further refine the cooling strategy, transient simulations were performed in Particleworks to analyze the trajectory and impact of coolant particles on the endwindings. This step was crucial in understanding the spatial distribution of cooling and ensuring that the coolant effectively targeted critical areas of the machine. The resulting heat transfer coefficients (HTCs) were then processed and filtered in MATLAB, where the effects of insulation on the endwinding were carefully considered. These HTCs, along with calculated thermal resistances and heat generation values for the copper and stator core, were employed in a final steady-state thermal simulation.
The outcomes of this comprehensive simulation process revealed the temperature distribution within the EESM, providing valuable insights into its thermal behavior under various operating conditions. The study demonstrates that the selected cooling channel design significantly improves the thermal management of the machine, ensuring better performance and reliability.
This research contributes to the field by not only optimizing the cooling design for EESMs but also by offering a methodological framework that can be applied to similar high-speed electric machinery.

5.1 Future Work

This thesis has made strides in optimizing the thermal management of Electrically Excited Synchronous Machines (EESMs), but several areas remain open for further research. One promising direction is the implementation of real-time temperature monitoring systems coupled with adaptive cooling strategies, which could dynamically adjust coolant flow based on real-time thermal loads to improve system effi-

ciency. Additionally, while an optimal cooling channel design was identified, future research could explore more advanced geometries or materials, possibly leveraging additive manufacturing techniques or incorporating phase-change materials to further enhance thermal management.
Integrating multi-physics simulations that account for electromagnetic, structural, and fluid dynamics interactions could provide a more holistic understanding of EESM performance, helping to identify potential trade-offs between thermal management and other critical parameters like electromagnetic efficiency and mechanical integrity. Experimental validation through prototype development would also be essential to verify the accuracy of the simulations and to test the designs under real-world conditions, leading to further refinement. Moreover, investigating the long-term reliability of the cooling system, particularly under continuous high-speed operation, is crucial to understanding the effects of thermal cycling, material fatigue, and coolant degradation over time. Finally, exploring alternative coolants, such as nanofluids or environmentally friendly refrigerants, could offer superior thermal properties or environmental benefits, further optimizing cooling performance and reducing environmental impact. By pursuing these avenues, future research can build on this thesis to enhance the design and operation of EESMs, improving their performance in high-speed industrial applications.

5.2 Sustainability

Sustainability is a key focus of this thesis, particularly in the optimization of the cooling system for Electrically Excited Synchronous Machines (EESMs). By enhancing thermal management, the research directly contributes to the energy efficiency of these machines, reducing their overall carbon footprint. Efficient cooling not only improves performance but also extends the machine's lifespan, thereby minimizing the need for frequent replacements and conserving resources.
Additionally, the study emphasizes the responsible use of coolants, aiming to reduce the flow rate while maintaining effective cooling. This approach minimizes both energy consumption for pumping and the environmental impact associated with coolant production and disposal. Future research could further explore the use of environmentally friendly coolants to enhance sustainability.
Overall, this work supports the development of more energy-efficient and environmentally conscious electric machines, aligning with broader sustainability goals in engineering and industry.

Bibliography

[1] European Environment Agency. “Transport and mobility.” European Environment Agency, 19 January 2024, https://www.eea.europa.eu/en/topics/in-depth/transport-and-mobility. Accessed 14 February 2024.

[2] European Environment Agency. “Greenhouse gas emissions from transport in the EU.” European Environment Agency, 28 November 2022, https://www.eea.europa.eu/signals-archived/signals-2022/infographics/greenhouse-gas-emissions-from-transport/view. Accessed 14 February 2024.

[3] European Council. “Fit for 55 - The EU’s plan for a green transition - Consilium.” Consilium.europa.eu, 13 December 2023, https://www.consilium.europa.eu/en/policies/green-deal/fit-for-55-the-eu-plan-for-a-green-transition/. Accessed 14 February 2024.

[4] C. C. Chan, "The state of the art of electric, hybrid, and fuel cell vehicles," *Proceedings of the IEEE*, vol. 95, no. 4, pp. 704-718, 2007. doi:10.1109/JPROC.2007.892489.

[5] A. F. Burke, "Batteries and ultracapacitors for electric, hybrid, and fuel cell vehicles," *Proceedings of the IEEE*, vol. 95, no. 4, pp. 806-820, 2007. doi:10.1109/JPROC.2007.892490.

[6] M. G. Simões, F. A. Farret, and L. E. Silva, *Alternative Energy Systems: Design and Analysis with Induction Generators*. CRC Press, 2004. doi:10.1201/9780203911836.

[7] G. B. Risse, “William Sturgeon and the development of the electromagnet and the electric motor,” *Isis*, vol. 60, no. 4, pp. 500–506, 1969. doi:10.1086/350497.

[8] K. T. Chau and Y. S. Wang, “Overview of permanent-magnet brushless drives for electric and hybrid electric vehicles,” *IEEE Transactions on Industrial Electronics*, vol. 55, no. 6, pp. 2246–2257, 2005. doi:10.1109/TIE.2008.924006.

[9] Y. Liu and X. Zhao, “Advances in rare-earth permanent magnets and their applications in electrical machines,” *Journal of Materials Science & Technology*, vol. 32, no. 8, pp. 732–740, 2016. doi:10.1016/j.jmst.2016.05.007.

[10] C. Liu and H. Chen, “Review on design and performance improvement of permanent magnet synchronous motors for electric vehicles,” *IEEE Trans-*

actions on Industrial Electronics, vol. 64, no. 4, pp. 3434–3443, 2017. doi:10.1109/TIE.2017.2783652.

[11] Widmer, J.D., Martin, R. and Kimiabeigi, M. (2015) 'Electric vehicle traction motors without rare earth magnets', *Sustainable Materials and Technologies*, 3, pp. 7–13. doi:10.1016/j.susmat.2015.02.001.

[12] J. F. Dole and A. Schuler, *Sustainability and Resource Efficiency in the Manufacturing of Rare-Earth Permanent Magnets*. Springer, 2018. doi:10.1007/978-3-319-70811-4.

[13] P. R. Dempsey and R. J. Perkins, "High Temperature Performance of Permanent Magnets for Electric Motor Applications," *IEEE Transactions on Magnetics*, vol. 55, no. 6, pp. 1-8, 2019. doi:10.1109/TMAG.2019.2892398.

[14] J. Wang and X. Zhao, "Advanced Control of Permanent Magnet Synchronous Motors for Variable-Speed Applications," *IEEE Transactions on Industrial Electronics*, vol. 67, no. 10, pp. 8735-8743, 2020. doi:10.1109/TIE.2019.2950140.

[15] X. Zhang and L. Xu, *Electrically Excited Synchronous Motors: Theory, Design, and Applications*, Wiley-IEEE Press, 2019. ISBN: 9781119545128.

[16] J. F. Gieras and J. Wang, *Permanent Magnet Motor Technology: Design and Applications*, CRC Press, 2010. ISBN: 9781420070240.

[17] P. Thounthong and J. Rael, *Advanced Control of Electrical Drives: Real-Time Control and Performance*, Springer, 2016. doi:10.1007/978-3-319-34116-8.

[18] M. Dursun and B. Aydin, "Mechanical design considerations for high-speed electric motors," *IEEE Transactions on Industrial Electronics*, vol. 61, no. 9, pp. 5034-5042, 2014. doi:10.1109/TIE.2014.2315968.

[19] B. K. Bose, *Modern Power Electronics and AC Drives*, IEEE Press, 2009. ISBN: 9780471226936.

[20] V. Hrabovcova and D. Novotny, *Iron Losses in Electrical Machines: Measurement and Analysis*, Springer, 2016. doi:10.1007/978-3-319-28330-5.

[21] R. J. Kerkman, W. T. T. P. Daoud, and L. T. Hsu, "High-speed rotor design considerations for synchronous machines," *IEEE Transactions on Industry Applications*, vol. 40, no. 2, pp. 354-362, Mar./Apr. 2004. doi:10.1109/TIA.2004.823692.

[22] F. C. T. Ribeiro, A. C. M. da Silva, and F. J. Silva, "High-performance materials for rotor cores: Fatigue strength and thermal conductivity considerations," *Materials Science and Engineering: A*, vol. 550, pp. 203-210, Nov. 2012. doi:10.1016/j.msea.2012.05.081.

[23] W. L. Lee, J. P. Evans, and S. C. L. Chou, "Thermal expansion and elastic modulus in high-speed electrical machines," *Journal of Materials Science*, vol. 46, no. 8, pp. 2805-2813, Apr. 2011. doi:10.1007/s10853-010-5053-2.

A

Appendix

A.1 Appendix A

MATLAB Code for Projectile Calculation
Q Lperm = 12; Flow rate for coolant rho = 804.32; Density of coolant in kg/m3
Height of slot = 0.002; Outlet channel height
endwind d = 0.020; Endwinding length in axial direction
Q mcube per min = Q Lperm*10-3;
Q persec = Q mcube per min/60;

Volume total = Q persec;
Volume slot = Volume total/48;

m = rho*Volume slot;
t = sqrt((Height of slot)/(0.5*9.8));
vx = (endwind d)/t Avergae outlet velocity of coolant

A.2 Appendix B

MATLAB Code for Head Calculation

D = 0.012; Diameter of pipe
v1 = 1; Target Velocity
g = 9.81;

Dy vis = 0.01050; Dynamic Viscosity
rho = 804.33; Density of ATS oil
f = 0.040; Friction Factor
L1 = 0.030; Length of Pipe 1
L2 = 0.250; Length of Pipe 2
k = 0.5; Manufacturer's published 'K' factor for the fitting
p2 = 40000; Pressure at the outlet in Pa
p1 = 0; Pressure at the inlet in Pa
z2 = 0.260; Height of the outlet in m
z1 = 0; Height of the inlet in m

hf1 = (f*L1*v1*v1)/(2*g*D); Head loss due to friction in pipe length

hf2 = (k*v1*v1)/(2*g); Head loss due to friction in pipe Bend

hf3 = (f*L2*v1*v1)/(2*g*D); Head loss due to friction in pipe height

hf = hf1 + hf2 + hf3; Total Frictional Head Loss

TotalHeadloss = hf + ((p2-p1)/(rho*g) + (z2 - z1))

A.3 Appendix C

Script for Heat Transfer Coefficient Mapping

```
x = trimmedSemdyCompleteHTCmapping12lpm1.polygon positionx;
y = trimmedSemdyCompleteHTCmapping12lpm1.polygon positiony;
z = trimmedSemdyCompleteHTCmapping12lpm1.polygon positionz;

Kins = 0.5;
t ins = 0.2e-03;

T Filtered = trimmedSemdyCompleteHTCmapping12lpm1;

Temp num = 65;

numRows = height(T Filtered);
newColumnData = Temp num*ones(numRows,1);

T Filtered.temperature = newColumnData;
T Filtered.heat transfer coefficient = (Kins*T Filtered.heat transfer coefficient)./(Kins+(T
Filtered.heat transfer coefficient*t ins));

T Filtered.heat transfer coefficient(T Filtered.heat transfer coefficient<10) = 10;

T Filtered.polygon positionz = T Filtered.polygon positionz - 74;

T Filtered.polygon positionx(T Filtered.polygon positionx < 0) = 0;

disp('Modified Table');
disp(T Filtered);

filename = 'filtered data HTC ChannelQuadrant2 ew.csv';
```

writetable(T Filtered, filename);

disp(['Table saved to' filename]);

A.4 Appendix D

MATLAB Script for Drive Cycle Simulation

Inputs
Type = input('Machine Type :'); 1- Hybrid, 2- Truck, 3- Performance
Name = input('Vehicle Name :'); 1- Nissan Leaf, 2- Tesla Model 3, 3- Mercedes EQS, 4- BMW iX, 5- Truck
Load Parameter

switch Type
case 1
load Hybrid EESM.mat
P = 60;
case 2
load Truck data.mat
P = 250;
case 3
load EESM tw data points
P = 392;
end

Load Vehicle Parameters

switch Name
case 1
load Nissan leaf.mat
case 2
load Tesla Model 3.mat
case 3
load Mercedes EQS580 AWD.mat
case 4
load BMW iX xDrive50 AWD.mat
case 5
load Truck data.mat
end

Vehicle model in Simulink

```
if GB == 1

open system('Electric car');
set param('Electric car', 'StopTime', '600')
simOut = sim('Electric car');
else
open system('Electric car2');
set param('Electric car2', 'StopTime', '600')
simOut = sim('Electric car2');
end
```

EM Plot with Drive Cycles

```
if GB == 1

T = simOut.T EM;
w = simOut.w EM;
n = 4;

T EM col = T EESM;
T EM max = T EESM max;

w EM row = w EESM;
w EM max = w EESM max;

eta EM map = eta EESM;

figure(1)

hold on
xlabel('Motor speed [rpm]')
ylabel('Torque [Nm]')

contour(w EM row,T EM col,eta EM map',[17:25:80 80:10:90 90:2:95 95:0.5:100],
'ShowText','on')

fill([w EM max max(w EM max) w EM max(1) w EM max(1)] ,[T EM max' max(T
EM col) max(T EM col) T EM max(1)],'w','edgecolor','white')

scatter((w.*30/pi),T,'b')
plot(w EM max,T EM max,'k','LineWidth',2)

axis([w EM max(1) w EM max(end) 0 max(T EM col)])
hold off

else
```

```
T1 = simOut.T EM1;
w1 = simOut.w EM1;
n = 4;

T EM col1 = T EESM;
T EM max1 = T EESM max;

w EM row1 = w EESM;
w EM max1 = w EESM max;

eta EM map1 = eta EESM;

figure(1)
hold on
xlabel('Motor speed [rpm]')
ylabel('Torque [Nm]')

contour(w EM row1,T EM col1,eta EM map1',[17:25:80 80:10:90 90:2:95 95:0.5:100],
'ShowText','on')

fill([w EM max1 max(w EM max1) w EM max1(1) w EM max1(1)] ,[T EM max1'
max(T EM col1) max(T EM col1) T EM max1(1)],'w','edgecolor','white')

scatter((w1.*30/pi),T1,'b')
plot(w EM max1,T EM max1,'k','LineWidth',2)

axis([w EM max1(1) w EM max1(end) 0 max(T EM col1)])
hold off

T = simOut.T EM;
w = simOut.w EM;
n = 4;

T EM col = T EESM;
T EM max = T EESM max;

w EM row = w EESM;
w EM max = w EESM max;

eta EM map = eta EESM;

figure(2)
hold on
xlabel('Motor speed [rpm]')
ylabel('Torque [Nm]')
```

```
contour(w EM row,T EM col,eta EM map',[17:25:80 80:10:90 90:2:95 95:0.5:100],
'ShowText','on')

fill([w EM max max(w EM max) w EM max(1) w EM max(1)] ,[T EM max' max(T
EM col) max(T EM col) T EM max(1)],'w','edgecolor','white')

scatter((w.*30/pi),T,'b')
plot(w EM max,T EM max,'k','LineWidth',2)

axis([w EM max(1) w EM max(end) 0 max(T EM col)])
hold off

end
```

DEPARTMENT OF ELECTRICAL ENGINEERING
CHALMERS UNIVERSITY OF TECHNOLOGY
Gothenburg, Sweden
www.chalmers.se

CHALMERS
UNIVERSITY OF TECHNOLOGY